Baikhati Elok Satiti

A Novel Study of Applying Indentation Plastometry on the WAAM Deposit

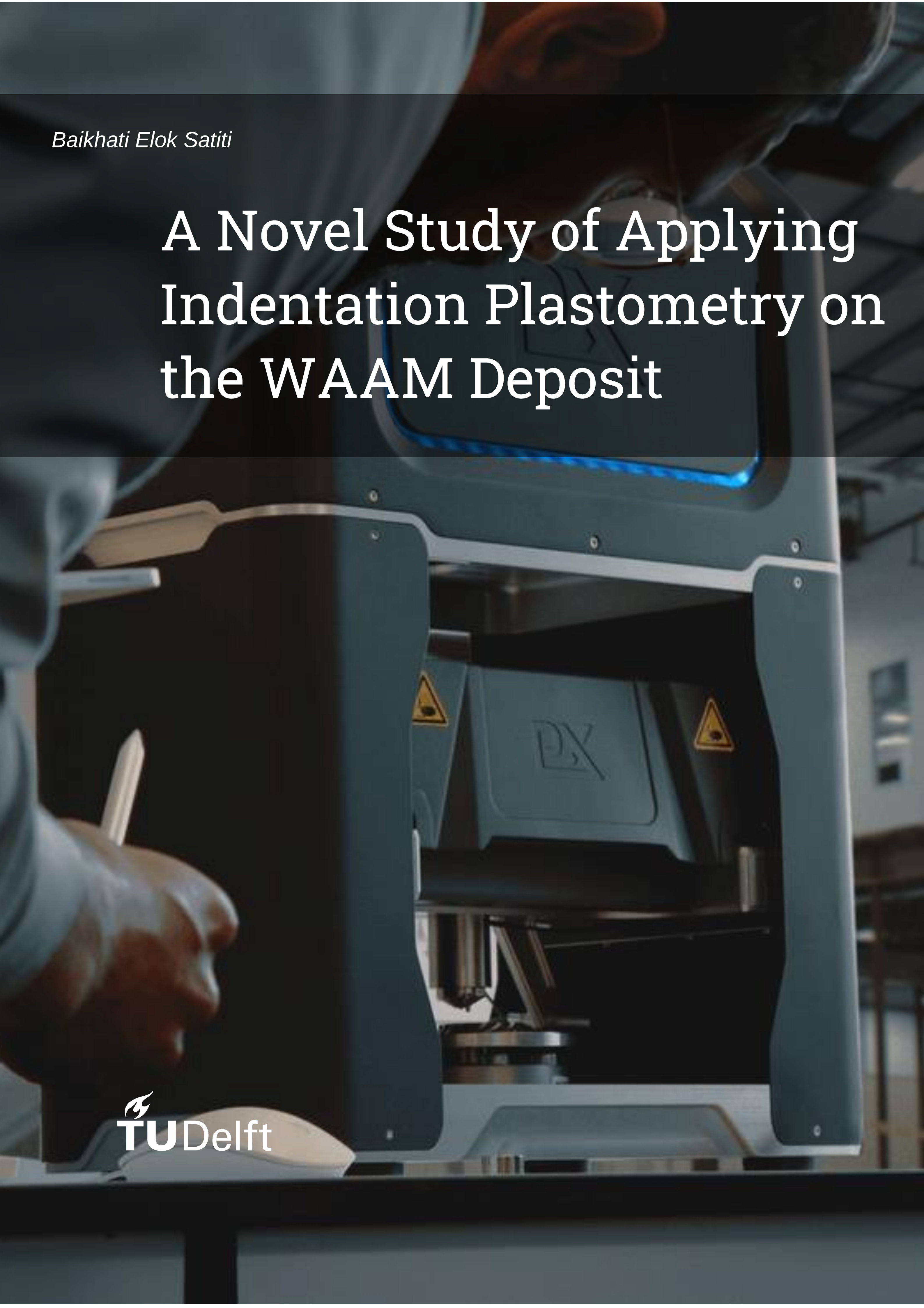

TU Delft

A Novel Study of Applying Indentation Plastometry on the WAAM Deposit

By

Baikhat Elok Satiti

in partial fulfilment of the requirements for the degree of

Master of Science

in Material Science Engineering

at the Delft University of Technology,

to be defended publicly on Wednesday October 30, 2024 at 10:00 AM.

Supervisor:	Dr.ir. M.J.M Hermans	TU Delft
	Dr.ir. Wei Ya	Ramlab
Thesis committee:	Dr.ir. Can Ayas	TU Delft

Acknowledgements

These past eight months have been both challenging and rewarding as I delved into wire arc additive manufacturing (WAAM) and gained practical experience with industrial applications. My time at RAMLAB has been invaluable, and I'm grateful to Vincent Wegener for giving me the chance to work on this project, as well as to the entire RDM family team for making my time there enjoyable.

I owe a special thank you to my company supervisor, Dr. Wei Ya. His guidance has been like that of a mentor, patiently helping me grow from the basics and always encouraging me to reach higher. His support has made a huge difference in my understanding of additive manufacturing and in the quality of this research. I feel incredibly fortunate to have had his mentorship throughout this journey. I am also grateful to Aditya, who was always there to answer my questions, tackle challenges with me, and offer wonderful friendship along the way.

I would also like to thank my university supervisor, Dr. Marcel Hermans, for his thoughtful guidance, which was essential in shaping this thesis into a polished final product. I am also thankful to Saskia, who, together with Dr. Hermans, provided great support not only with the technical aspects of this work but also with the administrative details that made this journey smoother. I am equally grateful to Remko and Durga, who were always willing to share their expertise and helped me improve my metallographic preparation skills at the TU Delft lab.

My heartfelt thanks go to my family for their unwavering support from afar, and to the Santosa family for making me feel at home in Delft. Lastly, I am deeply appreciative of my friends—Ardhito, Divakar, Sotoudeh, Prayla, Fahira, Aprisia, and many others—who have been a source of strength throughout my Master's program. I also extend my gratitude to the Indonesia Endowment Fund for Education (LPDP) for their financial support, which made this journey possible.

Baikhati Elok Satiti

Delft, October 2024

Contents

List of Figures

List of Tables

List of Abbreviations

AM	Additive Manufacturing
CMT	Cold Metal Transfer
DED	Directed Energy Deposition
FEM	Finite Element Method
GMAW	Gas Metal Arc Welding
GTAW	Gas Tungsten Arc Welding
HAZ	Heat-Affected Zone
HB	Brinell Hardness
HI	Heat Input
HV	Vickers Hardness
IN718	Inconel 718
ME	Material Extrusion
MR	Melting Rate
PAW	Plasma Arc Welding
PIP	Profilometry-based Indentation Plastometry
SAWP	Super Active Wire Process
TS	Travel Speed
UTS	Ultimate Tensile Strength
WAAM	Wire Arc Additive Manufacturing
WFS	Wire Feed Speed
WLAM	Wire Laser Additive Manufacturing
WEAM	Wire Electron Beam Additive Manufacturing
YS	Yield Strength

Abstract

This study explores the potential of using Profilometry Indentation Plastometry (PIP) to develop a methodology for guiding the process parameters optimisation in large-scale Wire Arc Additive Manufacturing (WAAM) deposits. The reliability of PIP measurements in evaluating the mechanical properties of WAAM deposits is assessed in comparison to traditional mechanical testing methods, while also examining how process parameters influence the microstructure and mechanical properties (material responses). The focus is more on the mechanical properties including the hardness, yield strength and tensile strength as the material (Mn Si alloyed steel solid wire, ER70S-6) investigated is well developed and studied in the literature.

The research focused on depositing sample using two deposition modes for investigating the material responses to the process. The two deposition methods are pulsed welding and Super Active Wire Process (SAWP) using a Gas Metal Arc Welding (GMAW) system from Panasonic. SAWP is a short circuit welding process working together with its mechanical push pull motor to manage heat input. A total of 119 samples were produced from single bead ramping tests, along with three larger blocks (250 mm × 90 mm × 250 mm) deposited using heat inputs of low, medium and high levels, respectively. The mechanical behaviour of the ramping samples was measured using a PIP device and then the measurements were analysed through curve fitting to find any potential physical trends. An exponential relation was found between the material response and the heat input. Additional single beads were also deposited on the substrate with different starting temperatures using a selected condition. This to simulate the bead deposition when depositing 3D block. Subsequently, the cross sections of these samples were prepared and measured using the PIP device. The trend curves then plotted with different exponential power index to find the correlation between the PIP measurements and the substrate starting temperature. These curve plotted together with PIP measurements of the samples extracted from the block deposited using different heat inputs, in which a good agreement was found. These results shown that it is promising to develop a systematic procedure that can correlate the single bead depositions with the large scale component to be deposited. The PIP measurements can help to reduce the R&D lead time

and to guide the parametric optimisation when using WAAM for 3D metallic printing. The power index value may have correlation with the cooling rate, as the resulting material properties are determined by the resulting microstructure, which depending on its chemical composition, grain size and orientation. These are interested aspects to be further investigated but cannot be included in this thesis.

Additionally, the obtained results also shown that the methodology of combining the single bead ramping together with the PIP measurement can effectively guide the selection of processing conditions and interpass temperature for larger WAAM deposits, which are important conditions to define the 3D printing procedure. Process parameters, particularly heat input, had a significant impact on the resulting mechanical properties of WAAM deposits, with a too high heat inputs, it can lead to reduced hardness. PIP hardness measurements shown a good agreement with the Vickers hardness measurements, and PIP strength measured shown reasonable agreement with the uniaxial tensile test results. It was noticed that yield strength measured using the PIP device shown the values systemically lower than the uniaxial measurements. This is likely due to limitations in the device’s fitting model inputs that has been predefined within the PIP device as a Blackbox towards the normal user. Further researches are expected to enable a better utilization of the PIP device to measure the WAAM deposits. Meanwhile it also expected that the device manufacturer (in collaboration with us in this thesis work) can further improve the device stability, accuracy and user friendliness based on our feedback that has been communicates. Nonetheless, the main research question of using PIP for assisting speed up of the process optimisation was successfully answered.

1 Introduction

Metallic Additive Manufacturing (AM) has garnered significant interest in recent years due to its design freedom and productivity in prototyping [1]. Among various AM processes, Wire Arc Additive Manufacturing (WAAM) stands out by combining traditional welding processes and AM principles. By utilizing standard welding machines, WAAM significantly reduces initial investment costs compared to powder-based methods [2]. One of WAAM's major advantages is the ability to create large components with high deposition rates and reduced complexity, making it particularly beneficial for industrial applications [3]. However, despite its potential, WAAM faces challenges, especially in dealing with complex geometries and material properties.

As with many other material processing technologies, process optimisation is crucial in WAAM as it can ensure process efficiency and deposition quality. It will be cost-effective throughout the manufacturing process if a material process window is available to guide the selection of the process parameters that are suitable for the desired product design and requirements. Typically, this optimisation is achieved through parametric studies, where small parts are investigated to identify the most effective parameters which are suitable for production with satisfactory material properties. These optimal parameters are then applied to the production of larger parts for further validation of material properties, which are typically mechanical properties such as strengths, elongation, hardness, *etc*. However, without a proper understanding of the material's responses to the process, this approach has limitations, as parameters optimised for smaller parts may not yield the same results when applied to larger components. The scale effect introduces complexities such as changes in the thermal cycles that material undergoes during WAAM deposition, which can have an effect on the resulting final material properties. Although some research showed WAAM's capability to create simple structures like blocks and walls [2, 4] with good material properties, applying this technology to actual applications often requires intricate modifications to process parameters, as the actual component is usually more complex in geometry. Therefore, it is often necessary to re-evaluate and fine-tune these parameters during the fabrication of larger parts to maintain the desired mechanical properties.

A comprehensive understanding of parameter modification for scale-up deposition with WAAM remains limited. This gap underscores the need for a methodology to guide the scale-up process from parametric studies to industrial large-size component deposition. Creating a processing window can help develop a better understanding of the material response to the process. It also helps defining operation boundaries for reliable production, ensuring that optimal properties' conditions can be achieved [5]. However, establishing a reliable process window is challenging, especially in 3D metallic printing using WAAM, as the material's response to different thermal cycles and the resulting material properties have not yet been fully investigated. This would require extensive, time-consuming, and expensive material testing. Some researchers [6, 7] have attempted to reduce the number of tests needed for process optimisation by combining process parameter ramping with hardness measurements. However, subsequent material tests, such as tensile testing, are still necessary to validate material mechanical property during the scale-up process. Additionally, iterations may be needed with this approach as hardness only provides a preliminary and semi-quantitative indication of material resistance to plastic deformation. In essence, the selected optimal process parameters may not be the true "optimal", raising the question of whether improvements can be made.

Driven by this question, this research set out to explore an approach that could be better and fast for process optimisation for WAAM applications. As we know that hardness can already provide sufficient indication of material strength, what is missing is the mechanical behaviour (the stress-strain relationship) of the deposit, measured in subsequent mechanical testing. Indentation plastometry can be helpful in this case, as indentation is much cheaper and more convenient compared to conventional tensile testing. Using an indentation-based procedure, the bulk mechanical properties of metallic materials in the form of the stress-strain relationships in the plastic regime, can be obtained. The idea of combining the indentation plastometry together with the ramping procedure to establish a reliable process window could shorten the process development time and lead to more guided process optimisation.

The conducted research work is summarized in this thesis as follows. A literature review is reported in Chapter 2 with relevant state-of-art of the topics addressed in this thesis. Chapter 3 details the methodology used in the research, outlining the experimental design, data collection, and analysis techniques. Chapter 4 presents the results of the study, including data interpretation and discussion of the findings. Chapter 5 concludes the thesis with a summary of the key findings and recommendations for future research.

2 State of Art

2.1 AM and WAAM Introduction

Additive Manufacturing (AM) offers several advantages over traditional fabrication processes. Unlike traditional subtractive manufacturing, which shapes products by removing material from an initial raw material block, AM creates products by adding materials incrementally, either layer by layer or surface by surface. This method allows for greater design flexibility, reduced waste and enhanced production efficiency [8].

In metallic AM, Powder Bed Fusion (PBF), Directed Energy Deposition (DED), and Material/Binder Jetting are more widely utilized as compared to other methods, such as Material Extrusion (ME), VAT Photopolymerization, and the Sheet Lamination Process, as illustrated in Figure 2.1 [9].

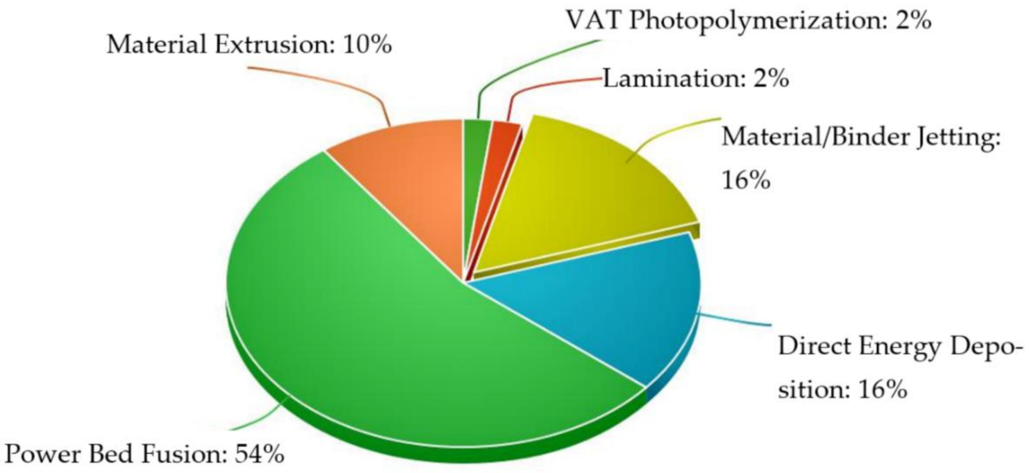

Figure 2.1 Metal Additive Manufacturing by Technology in 2020 [9]

Material/binder jetting processes offer the advantage of creating complex geometries with fine features using a wide range of materials. While material/binder jetting can produce fine features, DED and PBF, often achieve higher precision in terms of layer thickness, surface roughness, and minimum feature size. PBF is known for producing parts with finer details, superior surface finishes, and greater precision, whereas DED typically has a higher deposition rate, enabling reduced builds times. This makes DED the preferred choice for many industrial applications where speed and the ability to handle larger parts are crucial [10].

DED is classified based on the type of feedstock and the energy source used, as illustrated in Figure 2.2. On the one hand, powder-based DED can create complex precise parts, but is costly due to operational requirement/equipment (laser power), and material expenses (cost of making powder). Additionally, handling metal powders poses health risks, requiring controlled environments to prevent inhalation [11]. On the other hand, wire-based DED is more versatile since it can be operated with multiple energy sources such as an electric arc, laser beam, or electron beam. This flexibility leads to techniques like Wire Arc Additive Manufacturing (WAAM), Wire Laser Additive Manufacturing (WLAM), and Wire Electron Beam Additive Manufacturing (WEAM). Among these techniques, the electric arc is the most cost-effective, making WAAM attractive in industries [12].

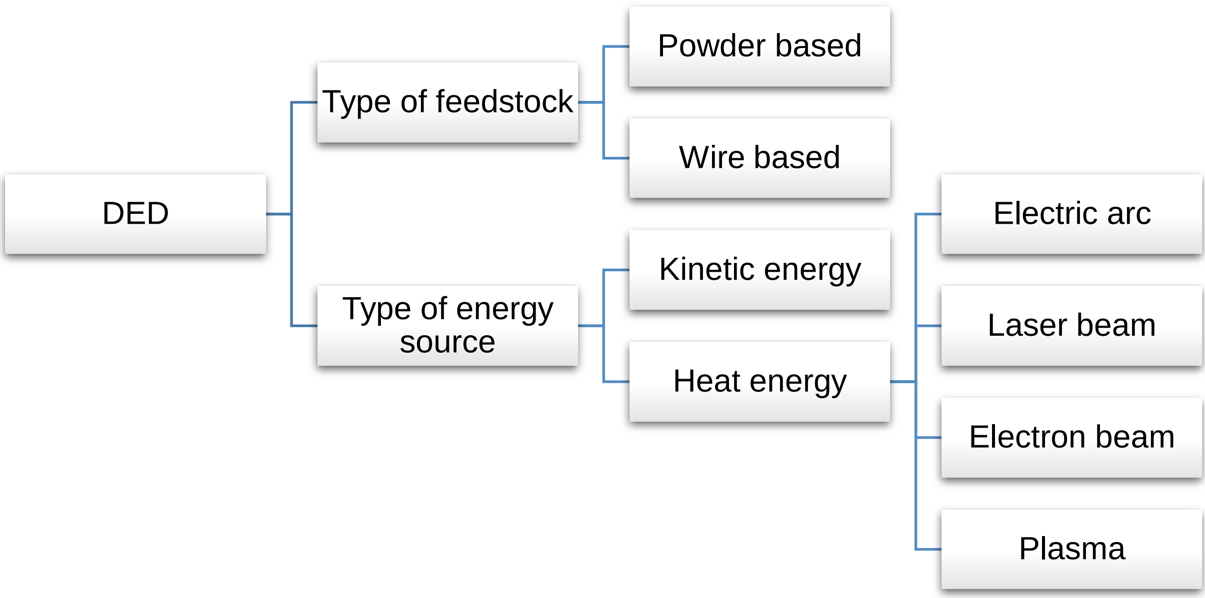

Figure 2.2 An overview of the DED classification

WAAM is based on traditional welding techniques, allowing the adoption of standard welding machines as energy sources. This lowers initial investment costs compared to powder-based methods and makes adoption easier in various industries having pre-existing application of welding techniques. Additionally, wire-type feedstock is about one-tenth the cost of powder-type materials [2], making WAAM more economically viable.

In WAAM, a wire is melted by an electric arc, and the molten material is transferred to a liquid metal pool where it cools and solidifies, forming the part layer by layer as the welding torch moves upward [11]. A typical representation of WAAM deposition is shown in Figure 2.3.

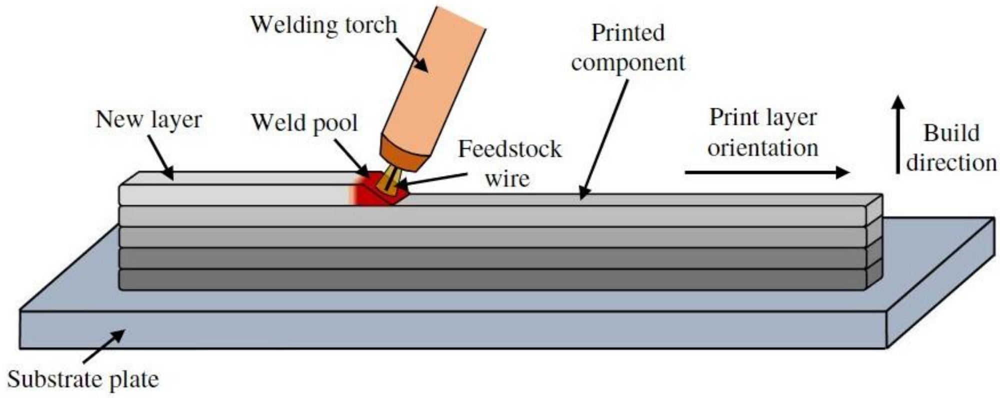

Figure 2.3 Schematic of the WAAM process [13]

When it comes to WAAM technology, different welding processes can be utilized, such as Gas Tungsten Arc Welding (GTAW), Plasma Arc Welding (PAW), and Gas Metal Arc Welding (GMAW). In GTAW and PAW, an arc is created between a non-consumable tungsten electrode and the workpiece, melting a separate filler metal wire, whereas GMAW involves an electric arc formed between a consumable wire as one electrode and a metal workpiece as the other electrode [5]. Schematic representations of all three processes are shown in Figure 2.4. The current study will be focused on deposits made using GMAW-based WAAM.

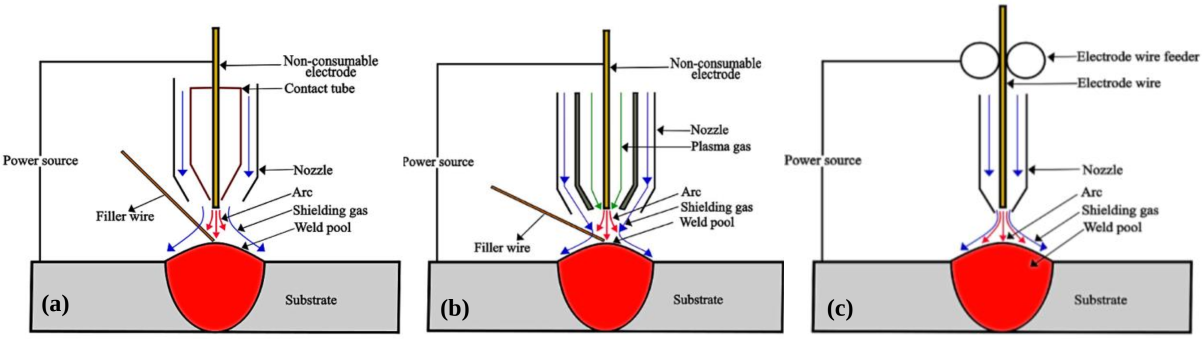

Figure 2.4 Types of WAAM: (a) GTAW, (b) PAW, and (c) GMAW [11]

2.1.1 Process Optimisation

As mentioned earlier, process optimisation in WAAM is essential for improving process stability. The goal is to produce high-quality deposits at reduced costs by fine-tuning controllable process parameters [15]. While modelling techniques such as Gaussian Process Regression (GPR) and other physical model-based machine learning methods [15, 16] can provide valuable insights, their effectiveness diminishes when the amount of data is limited. In such scenarios, experimental approaches are a fundamental and a direct method to generate reliable data and lay a good foundation for future research.

A common experimental approach involves single bead depositions with subsequent visual inspection. “Optimal” process parameters are often identified during this visual inspection. These single bead deposition conditions are then applied to larger-scale depositions, followed by full-scale testing of mechanical properties [1, 5, 13, 17]. However, the “optimised” single beads conditions often do not produce the same material properties when applied to larger depositions.

Kumar et al. [18] found that welding settings optimised for Inconel 625 single bead deposition using GMAW may not work well for overlapping beads because of interactions between them (single beads), such as heat buildup, uneven bead size, and inconsistent cooling. Similarly, Hussein et al. [19] showed that parameters suitable for single beads do not account for the buildup of heat in larger structures, meaning that recalibration is needed when performing GMAW on 308L stainless steel filler wire. Ding et al. [20] also pointed out that the shape of a single bead can lead to inconsistencies in multi-layer structures, requiring adjustments to the process settings when performed WAAM using mild steel.

2.1.2 Importance of Single Bead Deposition

Single bead deposition is the starting point in WAAM or any other fusion based deposition, as every surface or block structures are created by overlapping single beads. The single bead process conditions are the main factors influencing the resulting mechanical properties, dimensional accuracy, and structural integrity of the final components. Having a good-quality single bead improves process stability, interlayer bonding, minimising defects like delamination and porosity [21]. Along with a good toolpath design, it can offer an accurate dimensions of the build and a smooth surface finishing [22]. Additionally, since the final block deposit is formed from multiple overlapping beads, the resulting mechanical properties of the block are determined by the microstructure of these overlapping single beads, which experienced cyclic heat treatments during each bead deposition. Understanding the single bead characteristics is therefore important to prevent defects and ensure reliable properties, especially for the multi-layer deposition.

Evaluating the mechanical properties of single beads with material testing standard is challenging due to their limited size. However, the incorporation of dedicated testing equipment, as will be detailed in the following section, enables the measurement of single bead properties, allowing for better extrapolation and optimisation of parameters, which can be used to correlate the properties of the structures made with overlapped beads.

2.1.3 WAAM Process Parameter

WAAM relies on various process parameters, including welding current, arc voltage, travel speed (TS), wire feed speed (WFS), interlayer temperature, and heat input (HI). These parameters are important for achieving desired outcomes and minimising defects. Figure 2.5 provides a schematic illustration of the issues that arises when an improper combination of process parameters is used. For example, Figure 2.5(a) shows a bead produced with sufficient current, arc length, and speed. In contrast, if the current (measured in ampere) is too low, the weld may not have sufficient heat, resulting in poor penetration and weak bonding with the base metal as shown in Figure 2.5(b). When the current is too high, excessive heat cause spatter, small droplets of molten material ejected from the weld pool, which can be seen as spatter near the weld bead in Figure 2.5 (c). If the arc length is too short, as shown in Figure 2.5(d), it can result in excessive heat concentration, leading to an narrow, convex bead shape, which may cause poor fusion with the base material or during overlapping. If the arc length is too high, arc stability decreases, causing the arc to wander resulting in an irregular bead shape, as illustrated in Figure 2.5(e). The effect of travel speed is also significant. When the TS is too low, a large amount of material is deposited per unit length of weld, creating a wide melt pool as shown in Figure 2.5 (f). Conversely, at high TS the melt pool width becomes small, as seen in Figure 2.5(g).

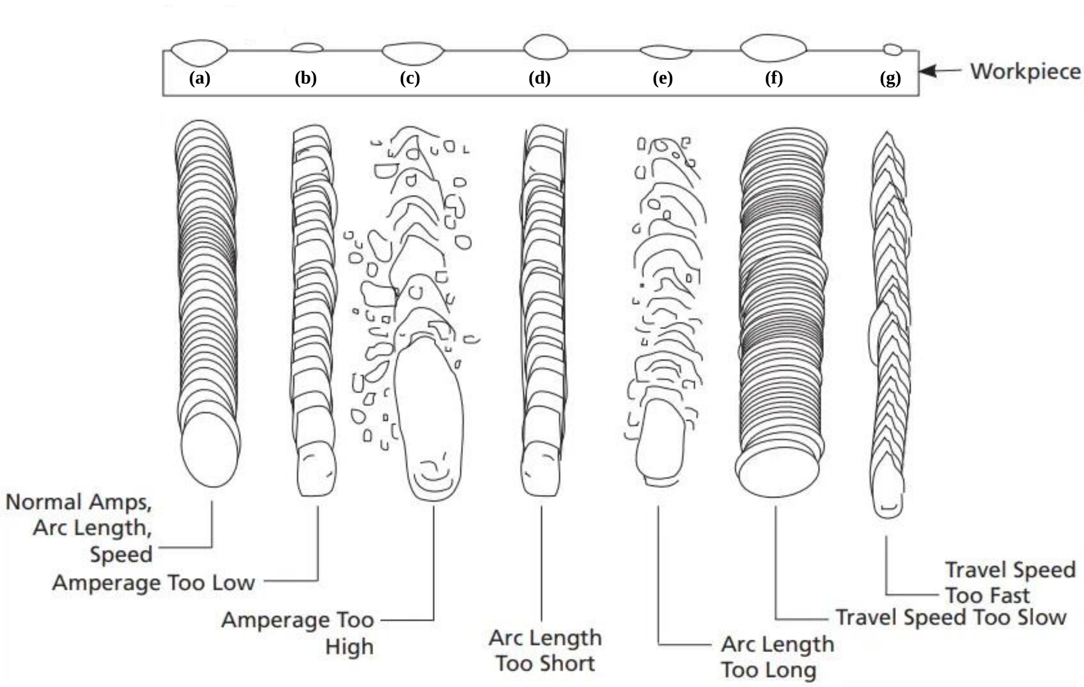

Figure 2.5 Overview of the effect of welding process parameters on the weld quality [23]

Heat Input

Heat input is an important factor that determines the final microstructure, mechanical properties, and residual stresses of components produced using WAAM [21, 24, 25]. It is a comprehensive indicator of thermal energy, influenced by several welding parameters, including voltage, current, and travel speed. Variations in heat input can cause changes in microstructure and mechanical characteristics due to phase transformations under different cooling rates induced by varying heat inputs. For instance, Babu et al.[26] demonstrated that reducing heat input can increase the martensite phase fraction, enhancing strength and hardness, when depositing high-strength steel (S690 grade) using Cold Metal Transfer (CMT).

In multi-layer structures the material experiences multiple thermal cycles during layer-by-layer deposition [11]. Repeated thermal cycling in materials such as steels can cause tempering effects, reducing hardness by transforming martensite to tempered martensite or ferrite. In aluminium alloys, overaging may occur. Additionally, higher heat input can cause irregular deposits due to spatter, while lower heat input can lead to unstable arcs and non-uniform deposition as reported by Lee [2] in his work on depositing SS316L wire using CMT process.

The value of heat input can be calculated using Equation (1).

$$Heat\ Input = \frac{\eta UI}{TS} \qquad (1),$$

where U is the arc voltage [V], TS is the travel speed [m/min], I is the welding current [A], and η represents the arc thermal efficiency, assumed to be 0.8 in this study [27].

Travel Speed

Travel speed significantly affects material properties. As noted by Babu et al. [26] in the previous section, variations in heat input, which are influenced by adjustments in travel speed and interpass temperature, lead to different material properties. Figure 2.6 illustrates that higher travel speeds are associated with increased martensite formation in high-strength steel (S690 grade) wire deposition [26]. By decreasing the time each area is exposed to the heat source, higher travel speeds effectively reduce heat input and consequently affect the microstructure and mechanical properties of the deposited material [2, 28].

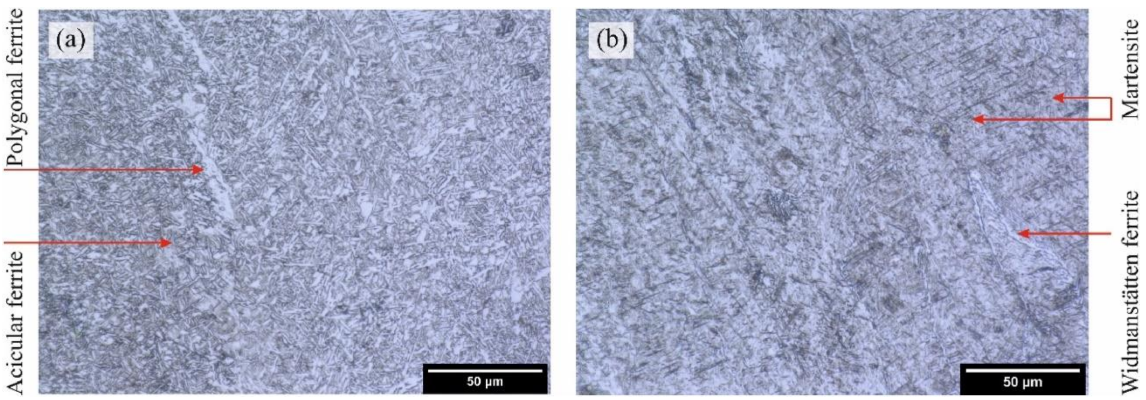

Figure 2.6 Optical micrographs of the beads deposited at different travel speeds in CMT process using S690 steel wire : (a) 8 mm/s and (b) 20 mm/s [26]

The shape of the weld bead is also significantly influenced by the travel speed. Research has shown that increasing the travel speed leads to a decrease in deposition layer width, as higher speeds resulted less metal to be deposited per unit area [30, 31]. Additionally, the travel speed also has an effect on bead height. At a fixed wire feeding speed, a lower deposition speed allows more material to accumulate in a single spot, resulting in a larger bead height, while a higher speed distributes the material over a larger area, resulting in a thinner bead [32]. Thus, selecting an appropriate travel speed is essential for achieving the desired aspect ratio or shape of the weld bead.

Voltage

Voltage measures the electric potential difference between two points in a circuit. In WAAM the arc voltage is defined as the voltage drop between the wire electrode and the workpiece. It plays an important role in determining the arc characteristics as it influences the arc length and stability as schematically shown in Figure 2.7. Higher voltages are in general associated with longer arcs. The arc length affects the heat input into the workpiece and the weld bead shape. A longer arc length can lead to increased heat input and wider weld beads. Too long arc should be avoided as already mentioned before and shown in

Figure 2.5(e).

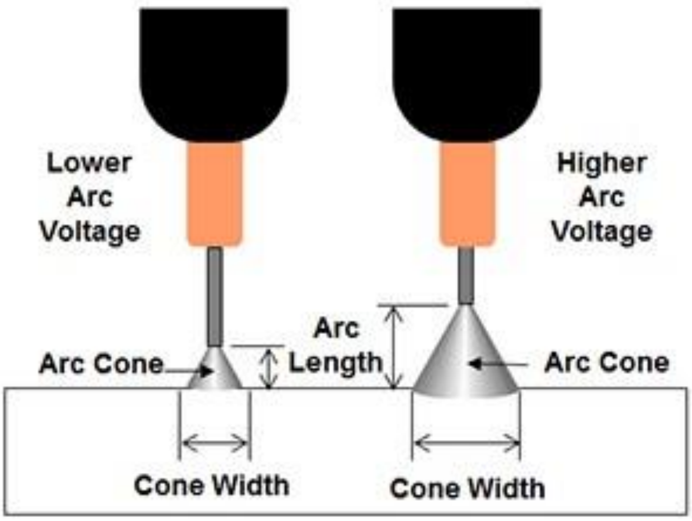

Figure 2.7 Effect of voltage on the arc characteristic [33]

Current and Wire Feed Speed

Welding current refers to the amount of electricity applied to melt the feed wire and substrate for proper bonding. Studies have shown that as welding current increases, bead height also increases in GMAW deposition of 308L stainless steel [32]. Decreasing current results in reduced penetration depth in GTAW-based WAAM of Hastelloy X alloy [1].

Welding current plays an important role in determining the stability of the welding process. As welding current increases, the amount of heat generated rises too, which affects the wire melting rate (MR). The wire melting rate should match to the wire feed speed (WFS), otherwise it will result in an unstable welding process. The wire MR [m/s] is related to the welding current (I) according to Equation (2) [34].

$$MR = aI + \beta l_e I^2 \qquad (2),$$

where α and β are constants that vary based on the wire's radius and other specific characteristics, I is the instantaneous welding current, which is defined according to the current waveform and is measured in amperes (A), and l_e is the represents the extension of the wire, expressed in meters (m). The first term on the right-hand side represents the contribution of arc heat and the second term on the right-hand sides represents the contribution of resistive (Joule) heating of the wire extension.

WFS is thus directly correlated with the welding current. Increasing the WFS requires a higher welding current as shown inFigure 2.8. Wu et al. [35] identified WFS as the second most significant factor influencing weld quality, following travel speed, in their CMT-P mode study on deposition using 2219 aluminium alloy. The relationship between WFS and travel speed has also been noted by Sun [5], emphasizing that both parameters must be adjusted together to prevent the formation of poorly shaped weld beads when using A-Fe-W 86 alloy wire deposition using CMT mode.

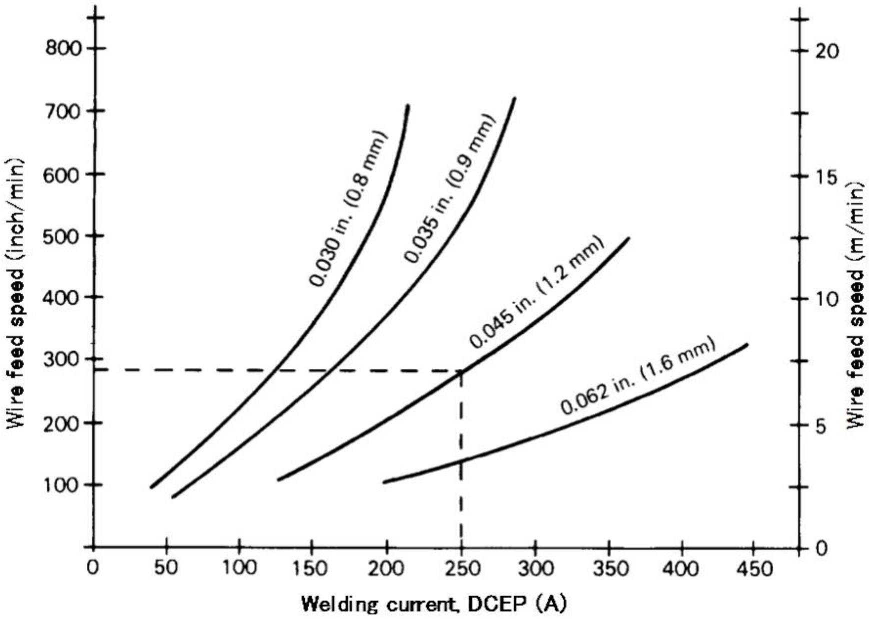

Figure 2.8 Typical welding current versus WFS for carbon steel electrodes [36]

2.1.4 Transfer Mode in WAAM

The mode in which the material is deposited onto the workpiece depends on the waveform and welding technique used. The material transfer mode during GMAW-based WAAM deposition can result in differences in mechanical performance of the as deposited material, particularly in terms of strength and ductility. Current research highlights that the transfer mode has influence on the heat input, deposition rate, and process stability. Panchenko et al. [37] reported that a controlled short-circuiting transfer mode results in lower heat input and improved properties for Ti-6Al-4V alloys compared to CMT and self-regulated metal transfer. Prado-Cerqueira et al. [38] demonstrated that CMT modes such as pulsed and advanced CMT, influence porosity and microstructure in AWS ER70S-6 mild steel wire with a copper coating, with CMT+A resulting in the highest tensile strength. Koppu [39] showed that transfer modes affect interfacial bonding quality in WAAM 316LSi stainless steel using cold metal transfer (CMT).

Two main transfer modes will be briefly reviewed as these transfer modes are used in this thesis. The two main categories of metal transfer are free-flight transfer and bridging/short-circuit transfer. In short-circuit transfer, the welding wire periodically touches the molten pool, creating a liquid bridge between the solid electrode wire and the melt pool. During the short circuit period the current increases, as does the associated Lorentz force. This force will finally rupture the liquid bridge, upon which the arc is reignited. This cycle is repeated 50 to 200 times per second [40] and results in a relatively low heat input. The other mode is pulsed transfer, which is a free-flight transfer mode using a pulsed current waveform that enables a controlled metal transfer process across a broad spectrum of heat and mass input levels. In this mode, a low base current sustains the arc while a high peak current melts the electrode wire, resulting in the continuous detachment of small droplets of molten material at an average current that remains below the threshold necessary for spray transfer [34].

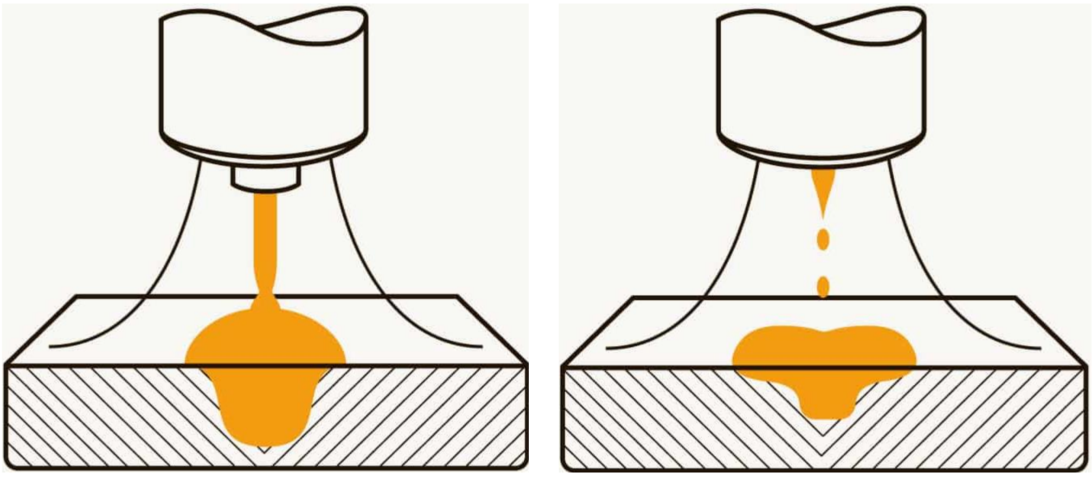

Figure 2.9 Main transfer mode in WAAM (a) short circuit transfer (b) pulsed transfer [41]

In this study two related transfer modes are applied: pulsed gas metal arc welding and super active wire process (SAWP). Pulsed welding/deposition mode is where the welding current alternates between a high current and a low current level. The peak current melts the electrode tip, creating droplets for deep penetration, while the background current helps solidify the weld pool and controls the heat input. SAWP, is a modified short-circuit mode where a servo motor controls and assisting the release of droplets by push and pull motion of the wire. During the short-circuiting phase, the motor retracts the wire, which helps break the liquid bridge more effectively than conventional short-circuiting. This mode allows for higher travel speeds without compromising bead geometry, resulting in improved production rates [40] .

2.2 Profilometry-based Indentation Plastometry (PIP)

Ultimately, printed parts should fulfil the designed requirements. If mechanical performance is defined, a wide variety of tests are available, ranging from hardness testing to tensile testing. A relatively novel technology to extract data is Profilometry-based Indentation Plastometry (PIP).

Profilometry-based Indentation Plastometry is an approach on determining the relation of metallic material stress and strain through an indentation experiment. It originated from an attempt to study the plastic deformation experimentally, beginning with the discovery of the first hardness test in the 19th century [42]. The initial method involved pressing a steel ball into a metal sample and measuring the indentation's diameter to determine its hardness. However, this method has limitations, as it depends on the indenter's size and shape and does not directly reflect fundamental plasticity characteristics such as yield stress and work hardening behaviour [42].

The uniaxial tensile test, as a refinement from the previous existing plastic deformation method provides a fundamental stress–strain curve that is considered a primary indicator of a material's plasticity characteristics as it can accurately represent material behaviour during plastic deformation [43]. However, conducting this test requires well-shaped samples, precise gripping techniques, and accurate strain measurement, all of which can be technically challenging [42]. Additionally, in-depth research involving an extensive number of samples can be relatively costly, as it requires at least three samples per variation to achieve accurate results. This also involves testing in multiple directions to account for anisotropy. With advances in technology in recent years, a new type of machine was developed to apply PIP for fast material plasticity characterization as shown in Figure 2.10.

Figure 2.10 Overview of the PIP device [42]

The method overcomes limitations associated with traditional uniaxial testing, where assumptions about uniform deformation can lead to inaccuracies, particularly in the presence of work hardening. To characterize work hardening from indentation testing, two common analytical expression used are the Ludwik–Hollomon (L─H) model and the Voce equation. The Ludwik–Hollomon (L─H) plasticity model is as follows:

$$\sigma = \sigma_Y + K\varepsilon^n \quad (3),$$

whereas the Voce equation is expressed as:

$$\sigma = \sigma_s - (\sigma_s - \sigma_Y)\exp\frac{-\varepsilon}{\varepsilon_0} \quad (4),$$

where σ is the applied (von Mises) stress, σ_Y is the yield stress, ε is the plastic (von Mises) strain, σ_s is the "saturation" stress level, and ε_0 is the characteristic strain indicating the approach towards the saturation level. In PIP, the Voce equation is preferred because it handles situations where the work hardening rate is very low, accurately describing materials with minimal work hardening [42]. This is preferred as not all steels have high hardenability [44–46].

In the process of obtaining a true stress–true strain relationship, three essential steps are involved [47]. First, a known force is applied to push a hard indenter into the sample as the crosshead moves downward, as shown in Figure 2.10. The known force is determined based on the material's elastic constants, including Young's Modulus and Poisson Ratio, which are input into the device before starting the test [42]. These values are pre-selected within the PIP system based on general material classifications, meaning users cannot manually adjust them. Young's modulus is selected from specific metal types menu, while Poisson's ratio is universally set to 0.33. These values are crucial because they define the material's elastic behaviour during the indentation process. However the sensitivity of the calculated plastic properties such as the true stress-strain curve, to changes in the elastic constants is generally low, as Young's modulus primarily influences the elastic portion of the indentation, while the inferred true stress-strain curve is mostly determined by the material's plastic behaviour. For instance, a ±10% change in Young's Modulus would result in only a small change in the final penetration depth, with minimal impact on the inferred plastic properties.

During the indentation process, a load-displacement plot is generated as the linear variable displacement transducer (LVDT) in the indenter housing measures the indenter's displacement relative to the sample. Following this, the indent's radially symmetric profile is measured using an integrated stylus profilometer, which scans the surface of the indent. After obtaining the experimental data (load-displacement curve and residual indent profile), the FEM simulation is run using initial elastic constants and an estimated set of Voce law parameters. The FEM predicts both the load-displacement curve and residual indent profile.

The predicted profile is then compared to the measured profile using a goodness-of-fit value S_{red} , which is calculated to assess the match. The goal is to minimise S_{red} , ensuring a close fit to the experimental data. If the match is poor, the FEM iteratively adjusts the Voce parameters until the simulated and measured profiles align [43]. The goodness-of-fit, or S_{red} , is calculated by Equation (5):

$$S_{red} = \frac{\sum_{i=1}^{N}(\delta_{i,M} - \delta_{i,E})^2}{N\delta^2{}_{av,E}} \quad (5),$$

where $\delta_{i,M}$ represents the modelled displacements from the FEM, $\delta_{i,E}$ is the corresponding experimental displacement, and $\delta^2{}_{av,E}$ is the average of all experimental displacements.

The PIP method requires minimal specimen preparation, as the minimal sample dimension for the biggest indent radius is 3 mm in thickness and 6 mm in lateral range. Therefore, it offers an alternative approach to characterizing material properties, particularly when the composition varies across the sample and there is limited availability of the tested material [48], such as in 3D-printed parts, where functional material is deposited and prototypes are often produced. It is convenient to have quick feedback on material properties, rather than conducting a full set of mechanical tests, which is time and resource-consuming. This has a major impact on the lead time of research and development.

The agreement of data between PIP measurements and uniaxial testing has been extensively investigated across various materials produced by casting and forging. However, few studies delve into materials produced using AM, especially deposits made using WAAM, as the commercial device has only recently become available. Tang et al. [49], in their research on ABD-850AM, and Southern et al. [50], in their study on Maraging Steel 300, both using laser powder bed fusion (LPBF) for sample fabrication, show that PIP results closely correspond to those obtained from standard tensile testing. Lancaster et al. [51] also reported good agreement between the properties obtained through PIP and uniaxial testing for wrought Inconel 718 (IN718) deposited using LPBF.

Limitation

Consistently minimal differences were also noted in a previous study on WAAM (Wire Arc Additive Manufacturing) deposits using PIP [52] particularly in yield stress values. This discrepancy is believed to be due to the FEM dataset being based on data from cast, forged, and rolled materials or other type of manufacturing techniques. These traditional manufacturing methods may result in properties that differ from those of AM materials, which undergo multiple thermal cycles and thus may show less uniformity. Another limitation is the current absence of a certified and standardized testing procedure due to the ongoing standardization process of this techniques. This lack of standardized protocols may contribute to the discrepancies observed in research findings, leading to variations in reported trends.

2.3 Motivation of the Thesis

Process optimisation is a important step during solution development when using WAAM for 3D printing. However, iterative and expensive material characterization and mechanical tests protocols can slow down or even hinder the whole innovation cycle. Could we combine the development of the process window with the PIP technique to shorten the lead time for research and development? This would involve integrating process parameter window development with material responses (bead characteristic + PIP measurements), allowing for an overview of how materials respond to the process. This approach can help navigate process parameter optimisation for specific applications. Driven by this idea, the following research questions being proposed and investigated in this thesis.

1. How can Profilometry Indentation Plastometry (PIP) be applied to develop a new methodology to guide for process optimisation in Wire Arc Additive Manufacturing (WAAM) deposits?
2. Are PIP measurements reliable enough to replace traditional mechanical testing for assessing WAAM deposit properties?
3. How do process parameters influence the microstructure and mechanical properties of WAAM deposits, and what is the correlation between these factors as revealed by metallurgical analyses and PIP measurements?

3 Experiment Design

In this chapter, parametric experiments are described that were designed to study the effects of the process parameters and size difference on the quality of the resulting deposits. There are two size categories specified: single beads and 3D block deposits. The experimental setup used for the deposition is introduced below.

3.1 Experimental Setup

A Panasonic WGHIII-E-HH020L welding system from Valk Welding with a Siegmund welding table was used to perform the single bead deposition experiments as shown in Figure 3.1 . The shielding gas used was Ferromaxx® Plus (12 % CO_2, 20 % He in Argon) at the flow rate of 20 L/min.

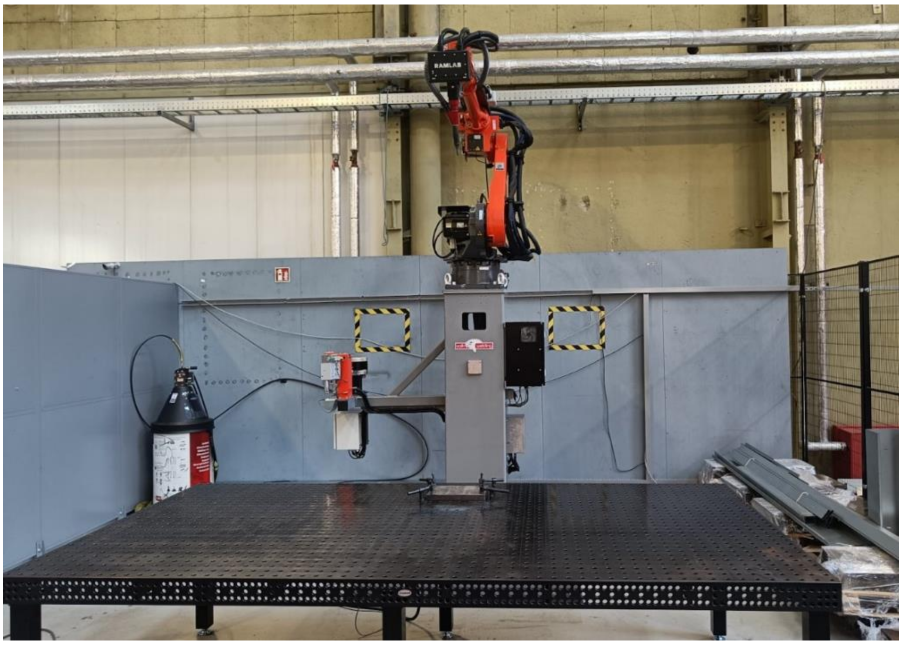

Figure 3.1 Panasonic WGHIII-E-HH020L robot setup for printing experiments

Another Panasonic TM 2000 WGIII welding system with an external manipulator was also employed in the experiment for block deposition. A fan was used for active air cooling to account for the longer cooling time for larger deposits. In this experiment as well, Ferromaxx® Plus was also used as shielding gas with a flow rate kept at 20 L/min. The overview of the wall printing setup is shown in Figure 3.2.

Figure 3.2 Panasonic TM 2000 WGIII robot setup for printing experiment

3.2 Material Used

S355J2 steel base plate and G3Si1 welding wire

The S355J2 steel base plate ($300 \times 200 \times 30$ mm^3 and $250 \times 60 \times 10$ mm^3) was used. S355J2 is a high-strength, low-alloy structural steel that is commonly used in civil construction. Its advanced performance allows it to meet rigorous construction specifications while cutting down on material use and expenses. The chemical composition of this steel base plate is given in Table 3.1.

Table 3.1 Chemical composition of S355 Structural Steel [53]

Element	C	Si	Mn	P	Cu	S	Fe
[wt.%]	0.2	0.55	1.6	0.025	0.55	0.025	Bal.

G3Si welding wire, with a diameter of 1.2 mm was used as a feedstock. The chemical composition of this wire is given in Table 3.2.

Table 3.2 Chemical composition of G3Si1 filler material [54]

Element	C	Si	Mn	P	S	Cu	Fe
[wt.%]	0.088	0.9	0.50-1.50	0.10	0.50	0.19	Bal.

3.3 Experimental Details

3.3.1 Single Bead Deposition Strategy

To generate a comprehensive dataset, a ramping deposition strategy was employed. This approach allows the examination of a wide range of welding conditions by varying heat inputs, using less material and fewer test runs [55]. The experiments were designed to provide an overview of material responses to the process, so that a meaningful process window could be established for guiding follow-up industrial engineering optimisation, which will be not be included in the current research. The experiments involved single bead deposition, where one parameter, such as voltage, was varied along the length of the deposition, while other parameters like wire feed speed, current, and travel speed remained constant. This variation resulted in different bead geometries within a single weld bead. A schematic representation of the ramping test is provided in Figure 3.3. Eight speed ramping (with speed variation, constant current and voltage) tests were conducted in pulsed mode, while nine tests were performed in Super Active Wire Process (SAWP) mode. Each test number, aligned vertically, underwent energy ramping where speed remained constant, but current and voltage were varied. Each step runs horizontally along the test number. An overview of the ramping tests is presented in Figure 3.4, with detailed test parameters listed in Table 3.3 and Table 3.4. To ensure an accurate reflection of the material's response, the bead was deposited when the plate's temperature was below 50°C (room temperature). The effect of preheat temperature on bead formation is discussed in section 3.3.3.

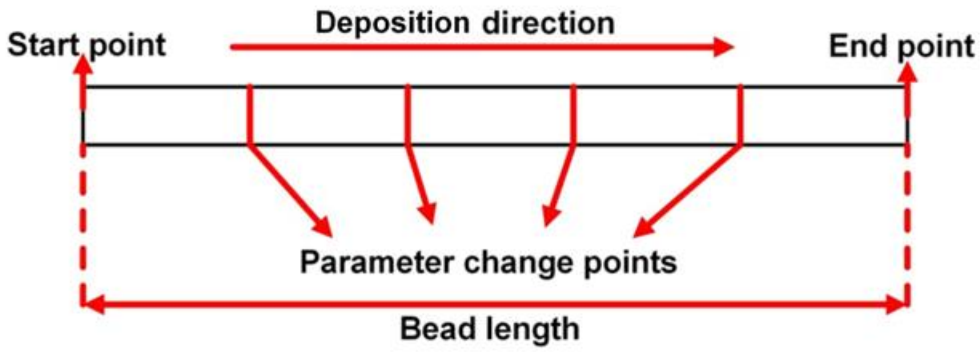

Figure 3.3 Schematic of ramping deposition [56]

Figure 3.4 Overview of the ramping test of the single bead

Table 3.3 Constant current and voltage with ramped up speed for Pulsed mode

Test Number	WFS Low	WFS High	Voltage Low	Voltage High	Travel Speed	WFS Interval
	m/min	m/min	V	V	m/min	m/min
Test 1	3	13	22.4	31.4	0.5	1.6
Test 2	4.5	14.5	24.3	33	0.75	1.6
Test 3	4.5	14.5	24.3	33	1.00	1.6
Test 4	4.5	14.5	24.3	33	1.25	1.6
Test 5	4.5	14.5	24.3	33	1.50	1.6
Test 6	4.5	14.5	24.3	33	0.75	1.6
Test 7	10	16	29.6	35	0.75	1
Test 8	3	15	22.4	33.6	0.25	2

Table 3.4 Constant current and voltage with ramped up speed for SAWP mode

Test Number	Voltage Low (V)	Voltage High (V)	Current Low (A)	Current High (A)	Travel Speed (m/min)	Current Interval (A)
Test 1	14.3	19.5	80	320	0.50	40
Test 2	14.3	19.5	80	320	0.75	40
Test 3	14.3	19.5	80	320	1.00	40
Test 4	14.3	19.5	80	320	1.25	40
Test 5	14.3	19.5	80	320	1.50	40
Test 6	14.3	19.5	80	320	1.75	40
Test 7	14.3	19.5	80	320	2.00	40
Test 8	14.3	19.5	80	320	2.50	40
Test 9	14.3	19.5	80	320	0.25	40

3.3.2 3D Block Deposition

To assess single-bead parameters performance in large-sized deposits, block deposition was conducted. An alternating deposition direction between layers was applied where one layer was deposited from left to right, with overlapped beads, and the following layer from right to left with overlapped beads. This approach was used to even out the height differences that happens at arc start/stop locations. Three distinct heat input levels were evaluated to observe how the variations influence the deposition outcome. The deposition details are presented in Table 3.5.

Table 3.5 Process parameter details for block deposition

Heat Input	**Interlayer Temperature (°C)**	**Actual Voltage (V)**	**Actual Current (A)**	**Travel Speed (m/min)**	**Heat Input (kJ/mm)**	**Dimension (T x L x H) mm^3**	**Deposition mode**
Low	120	18	175	0.7	0.216	90 x 300 x 250	SAWP
Medium	80	32.7	335	0.79	0.666	90 x 300 x 250	Pulsed
High	125	32.7	340	0.5	1.067	90 x 250 x 250	Pulsed

3.3.3 Single Deposition on Substrate with Different Temperatures

Substrate temperature during deposition can have an influence on microstructure development and the final properties of the deposited mild steel. In this study, samples were deposited on substrate at four different temperatures: 25 °C, 50 °C, 100 °C, and 200 °C. The same heat input was used for later comparison of the material response. The variation in substrate temperatures is expected to have an influence on the resulting microstructure and material properties.

3.3.4 Sample Preparation

Post-deposition, the single beads were prepared for detailed analysis using standard metallurgical procedures, including cutting, mounting, grinding, and polishing. Cross-sections of the samples were etched with 2% Nital (98% ethanol and 2% HNO_3) for reviewing the microstructural. Meanwhile the 3D block was outsourced to Element B. V. for performing follow up microstructural examination and mechanical tests. Only the uniaxial test and hardness test data were collected and used in this thesis.

3.3.5 Bead Characterization

Understanding the deposited bead geometry is of prime importance for 3D printing using WAAM [28]. To characterize weld bead geometry, a cross-sectional view of the weld bead was investigated, as shown in the example in Figure 3.5 where a single bead was deposited using pulsed mode with 0.693 kJ/mm heat input. This cross-section allows for the measurement of bead width, bead height, and penetration depth, which will be used for later analysis. The cross-sectional micrograph of the weld bead was performed using optical microscopy with the Keyence VHX-5000 Digital Microscope from Osaka, Japan. The spherical shape shown in Figure 3.5 is the indent mark left from the PIP measurements.

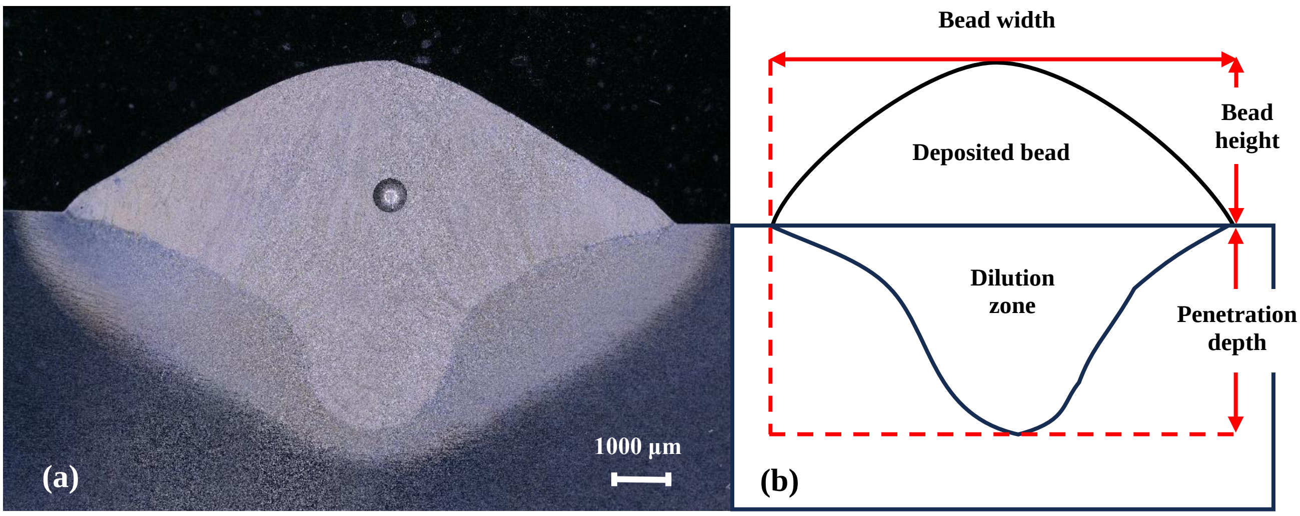

Figure 3.5 Single bead cross-section deposited at 250.55 A, 28.81 V and deposition speed of 0.5 m/min (a) micrograph (b) schematic drawing

3.3.6 Mechanical Properties

For all the single beads, the Vickers hardness (H_V 0.5, with 0.5 kgf) was assessed using a DuraScan - Microhardness Tester from Struers Inc. in Westlake, USA. Additionally, Indentation Plastometry analysis was performed using a Profilometry-based Indentation Plastometry (PIP) device from Plastometrex, headquartered in Cambridge, England. For these measurements, the specimen surfaces were carefully polished before testing. An 0.5 mm indenter radius was used and the material specification input was set to Steel and Steel alloys. Before the indentation test, a full calibration of the PIP device was performed.

4 Result & Discussion

In this chapter, the experimental results are presented, including analyses, data interpretations and their correlation to the research objectives. Discussions are made in each section based on the observations.

4.1 Effect of Process Parameters on Weld Geometry

The deposited beads across a wide range of heat inputs for two different deposition modes are presented in Figure 4.1 and Figure 4.2. A total of 119 variations of heat input are obtained ranging from the lowest 0.032 kJ/mm up to the highest 2.36 kJ/mm. As shown in the figures, most of the beads are continuous with no evidence of instability, except for test 9, step 1 (highlighted in yellow), which was due to a very low heat input that can cause discontinuity of the bead. The bead differences between the Figure 4.1 and Figure 4.2 are attributed to the different welding modes that were used. The pulsed mode typically operates at a higher welding voltage to keep the arc continuously 'on' throughout the process, resulting in more arc energy, which helps to spread the bead in most steel alloys. In contrast, the Super Active Wire Process (SAWP), developed by Panasonic, is a type of cold metal transfer mode. It operates in short circuit mode and works with a dedicated motor to control the push-pull motion of the wire, allowing for better heat input control and significantly reducing spatter compared to traditional short circuit modes.

Figure 4.1 Bead appearance from ramping test in pulsed mode

Figure 4.2 Bead appearance from ramping test in SAWP mode

Cross-section of the beads deposited using the different deposition mode

The bead characteristics (bead width, bead height, heat-affected zone (HAZ), and penetration depth) can be analysed through optical microscopy on the cross-section cut of the bead laid. An example is shown in Figure 4.3, in which a representative cross-sectional micrograph compares bead characteristics at a similar heat input level of bead deposited using pulsed and SAWP modes, respectively. The pulsed bead was deposited using a heat input of 0.433 kJ/mm, and the SAWP bead has a nearly identical heat input of 0.434 kJ/mm. In pulsed mode the resulting bead, as shown in Figure 4.3(a) is wider and shows a larger penetration depth compared to the latter case. In SAWP mode, the resulting bead, as shown in Figure 4.3(b) is narrow and shows less penetration depth. Under the same magnification, the pulsed bead shows larger grains than the SAWP bead. The HAZ in the pulsed sample is larger than the SAWP sample. Detailed study on the HAZ was not performed in current study, as it does not have a major influence on the processing of the material investigated in this research.

To have a better understanding of the material responses to the process using different deposition modes, the cross-sections of the ramped sample at different heat inputs levels as shown in Figure 4.1 and Figure 4.2 were prepared and analysed. The results and discussion are presented in the following sections. The cross-sections are shown in Appendix A.

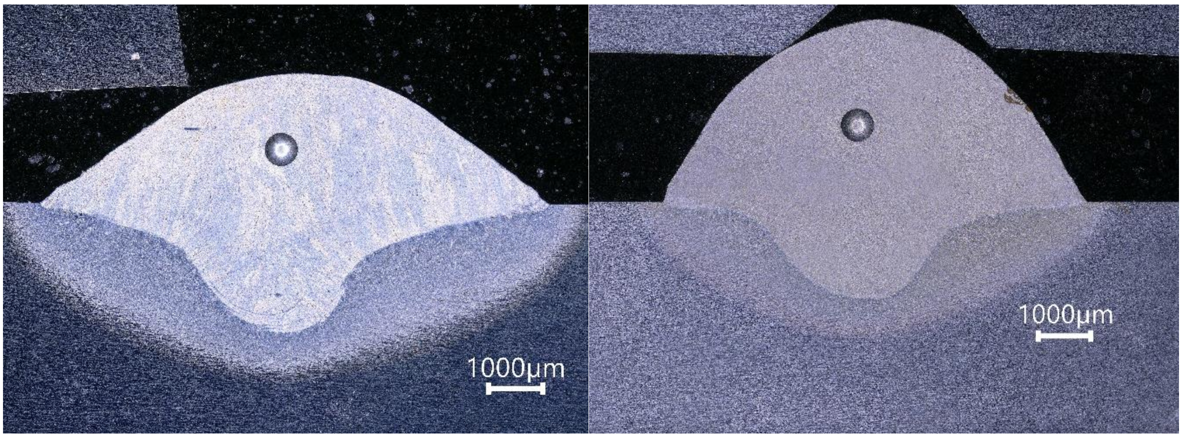

(a) (b)

Figure 4.3 Cross-sectional comparison of 2 mode of deposition in almost similar heat input (a) Pulsed (b) SAWP

Resulting bead characteristic using pulsed deposition mode

The effects of heat input on the resulting bead characteristics (bead width, bead height, and penetration depth) when using the pulsed deposition mode are shown in Figure 4.4. There are some interesting features that can be seen in the figures. In the pulsed case, as shown in Figure 4.4(a) and Figure 4.4(b), the increased heat input increases both the bead width and height. In the tested heat input range, it seems that both width and height shows a linear relation up to 1.6 kJ/mm, after which the influence on the bead width and height seems to be lesser. This may be due to the characteristic of pulsed welding, in which there is deeper penetration at higher heat input causes the melt pool to flow inwards [57], where the molten metal moves towards the centre of the weld pool beneath the surface, driven by thermal gradients and surface tension differences, enhancing penetration and weld quality, as shown in Figure 4.4(c).

At a fixed welding speed and based on the Equation (1), the penetration depth increases linearly with the heat input as shown in Figure 4.4(c). To have a better view of the speed effects in the penetration depth, Figure 4.4(d) is plotted with different colour that correspond to the ramping test as shown in Figure 4.2. In each ramping step, the current and the voltage were kept the same. It is now better visualized from both Figure 4.4(c) and(d), even at higher speeds, that the penetration can reach a certain depth (around 5 mm in this case) when there is sufficient heat input. Deep penetration was better achieved when depositing at higher speeds, where there would be less time for the heat transfer in the direction perpendicular to the deposition direction and less material would be fed into the melt pool. The low welding speed results in more material build up and encourages the spreading of the melt pool in the direction perpendicular to the deposition direction, as shown in Figure 4.4(a) and Figure 4.4(b). The electric arc supplies the heat input to the surface of the material (on top of the melt pool), this limits heat flow into the substrate, resulting in less penetration depth, as shown in Figure 4.4(c) and Figure 4.4(d). By understanding this, it can help better perform process optimisation when using the pulsed deposition mode.

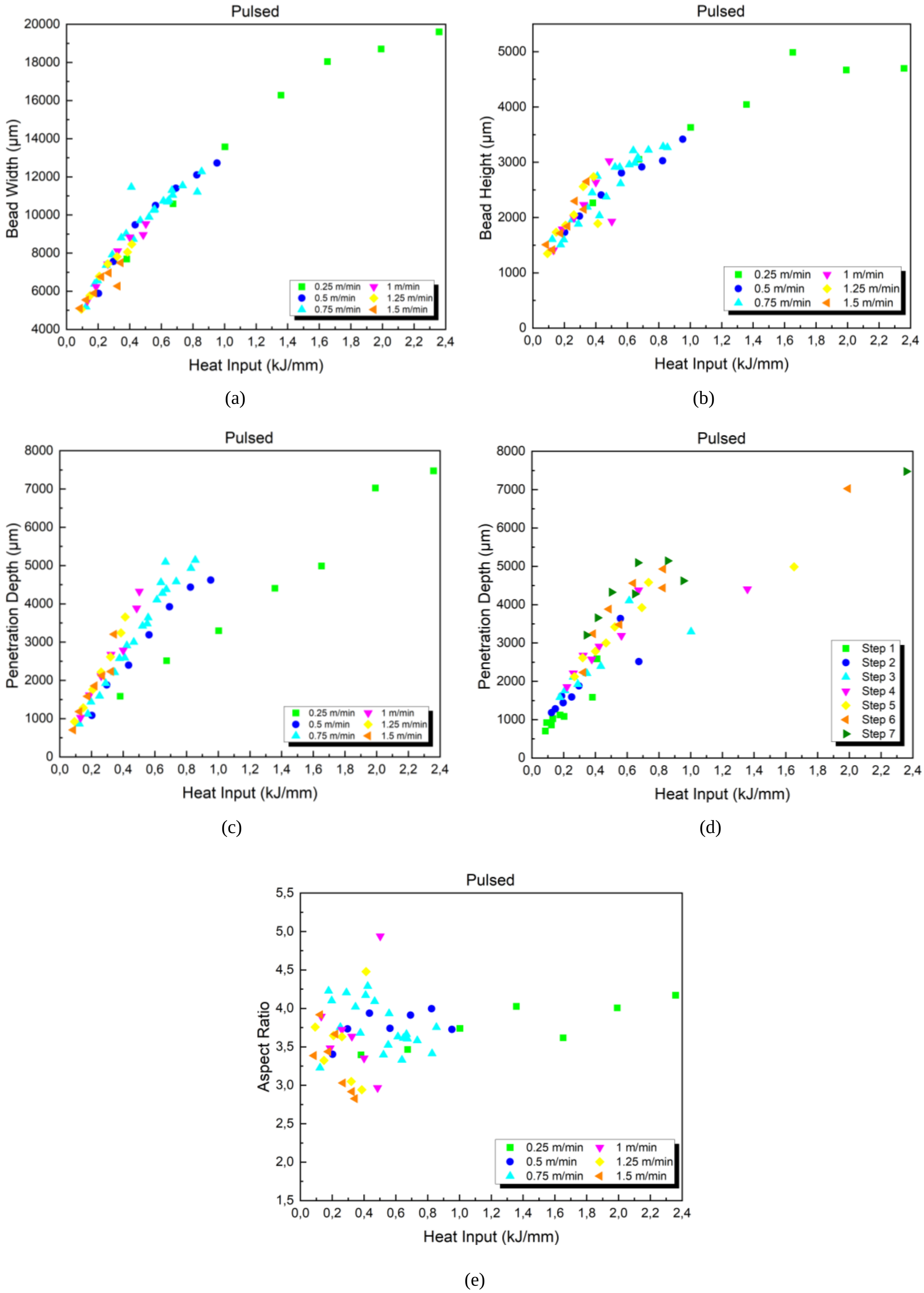

Figure 4.4 The effect of heat input on the resulting bead characteristics in pulsed mode (a) bead width, (b) bead height, (c) penetration depth, (d) penetration depth each step, and (e) aspect ratio

When applying the material for either 3D printing or surfacing, the aspect ratio (bead width divided by bead height) is used, as shown in Figure 4.4(e), this is commonly used for designing overlap beads in cladding [6]. To avoid inter-run-porosity during laser cladding, it is common to design the aspect ratio to be minimum of 4 [6]. However, during WAAM deposition, as long as the arc can reach the toe of a bead resulting in proper bonding, there is no specific required aspect ratio to be achieved. This is due to the physical differences between the two processes. In laser cladding, the bead shape can have a significant influence on the optical reachability of the laser spot, which provides the energy input. In contrast, in WAAM, the position of the electrode (feeding wire position) is more important, as the energy input is provided by the arc generated between the wire tip and the substrate. The current tends to conduct through the shortest route. The process optimisation is not within the scope of the current study. The current study provides sufficient information for further optimisation research activities being conducted in parallel.

Resulting bead characteristic using SAWP deposition mode

The effects of heat input on the resulting bead characteristics (bead width, bead height, and penetration depth) when using the SAWP deposition mode are shown in Figure 4.5. The increased heat input increases both the bead width and height as shown in Figure 4.5(a) and (b). The short circuit happens at around 100 Hz in which the arc on and off restrict the arc energy during the deposition. This resulted in a deposited bead that tends to be narrow and high. It can be seen from Figure 4.5(a) that the bead width is always restricted at different deposition speeds after a certain heat input level. Further increasing the heat input will only contribute to the height of the build-up, as shown in Figure 4.5(b). This is expected as the current has a positive relationship with the wire feed rate during GMAW [36]. Thus, the increased heat input contributes more to height build-up rather than encouraging bead spreading or increasing penetration. This can be observed from the Figure 4.5(c) and Figure 4.5(e), where the penetration appears to be limited after certain heat input levels at different welding speeds. The decreased aspect ratio as heat input increase, shows that the increased heat input contributes more to the height buildup of the bead. It is also interesting to note that the effect of welding speed on the penetration in this case is less compared to the pulsed mode, as shown in Figure 4.5 (c). Figure 4.5(d) shows that the penetration depth when using SAWP is more dependent on the heat input supplied, and deep penetration will be easier to achieve at low deposition speed. What is common between pulsed mode and SAWP is that the arc energy is generated between the electrode (feed wire) and substrate, which delivers the heat input from the surface of the generated melt pool. The main difference is that the pulsed mode will have a continuous arc and a concentrated heat flux delivered from the arc centre towards the melt pool. When depositing at higher speed, the melt pool will be thinner compared to depositing at lower speed. This thinner melt pool allows for easier arc penetration because there is less material between the electrode and the substrate. In case of SAWP, the penetration depends more on the heat conduction, as the arc heat flux is only effective during the arc-on period and not present during the short-circuiting period, therefore the process it is less influenced by the deposition speed. This become clear when comparing Figure 4.4(c) and Figure 4.5(c), and are combined in Figure 4.6. This means that at slow deposition speed and the same heat input, compared to the higher deposition speed, there will be a bit more time for heat conduction, which encourages penetration. This effect will be limited as speed increases. As the bead thickness increases, the penetration depth will be limited as well. These features make the SAWP an attractive process for 3D printing and superalloy surfacing [56], as the penetration can be well maintained. As mentioned earlier, the aspect ratio in this case too can be used to guide the process optimisation. However, there is no need to maintain a strict minimum ratio once a proper overlapping distance is found.

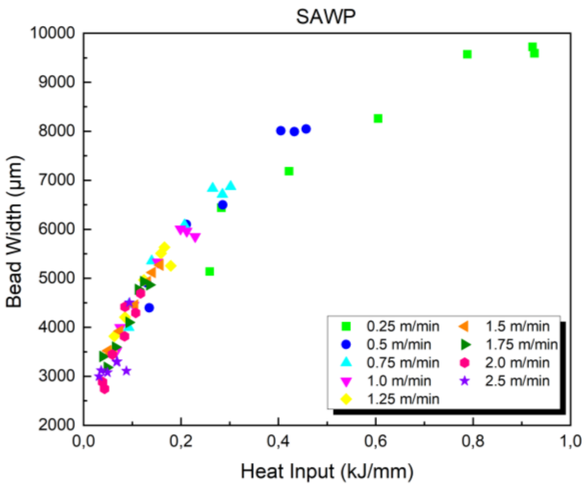

(a)

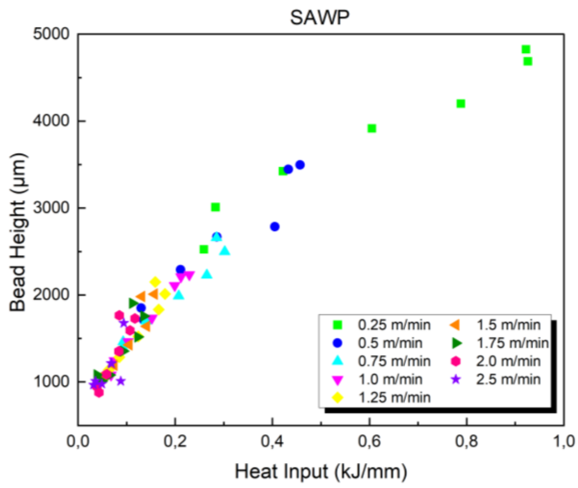

(b)

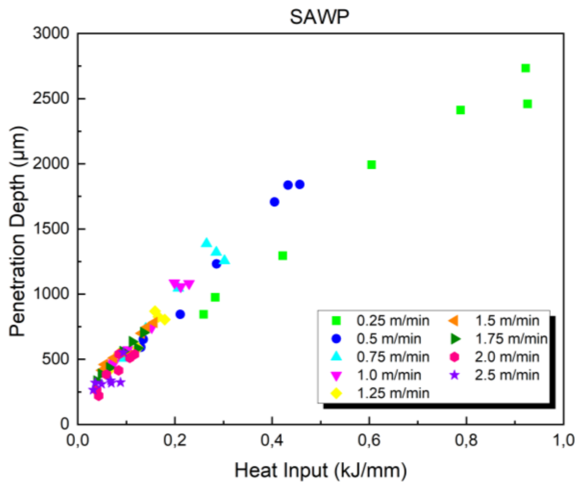

(c)

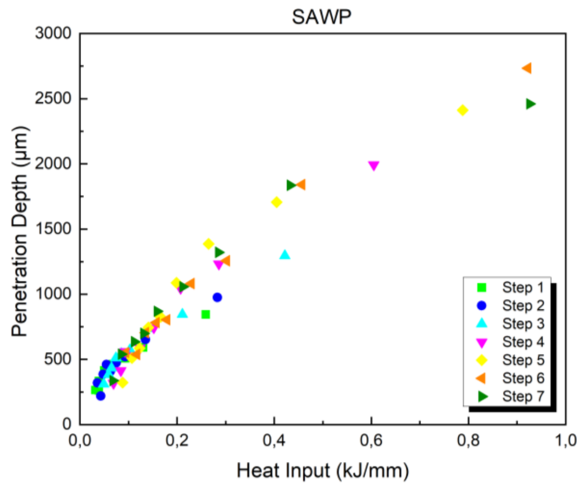

(d)

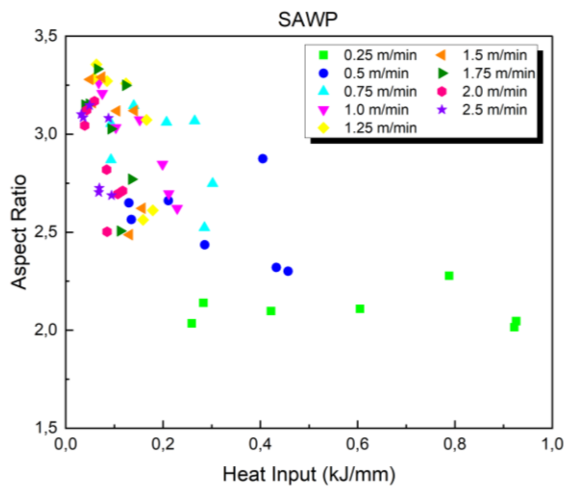

(e)

Figure 4.5 The effect of heat input on the resulting bead characteristics in SAWP mode a) bead width, b) bead height, c) penetration depth, d) penetration depth of each step, and e) aspect ratio

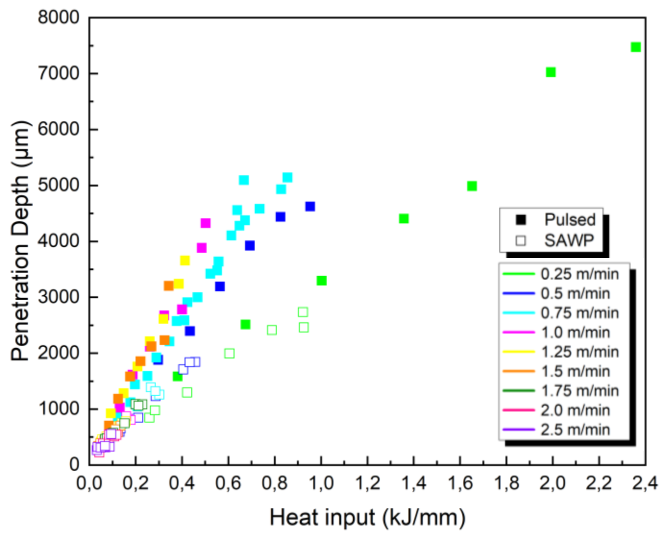

Figure 4.6 Penetration depth comparison for different deposition modes

4.2 Analyses of the Hardness and Strengths of Beads Measured Using the PIP Device

In this section the strength and hardness of single beads deposits subjected to various heat inputs are measured using the PIP device and analysed. The single bead weld provides a baseline understanding of the material behaviour under controlled deposition conditions. This approach allows for the observation of the material's response to heat input over a large range.

The experimental data for strength and hardness covers a moderate range, with yield strengths between 456 and 1167 MPa, tensile strengths ranging from 760 to 1303 MPa, and hardness values between 226 and 441 HB (equivalent to between 223 and 464 HV). The overview of material responses at different heat inputs is plotted in Figure 4.7, Figure 4.8 and Figure 4.9.

As shown in Figure 4.7, increasing heat input leads to a reduction in overall hardness. As the heat input increases, it will reduce the cooling rate, resulting in larger grains and hence lower hardness. This indicates that excessive heat during the deposition process can negatively influence the mechanical properties of deposit by reducing its strength. Babu et al. [26] reported that lower heat inputs result in higher hardness and material strength. It is also reported that an increase in the width of columnar grains as heat input rises [58] leading to a reduction in strength. In our case, the grain growth under higher heat input leads to a softer and weaker material, as the processed material is ferritic steel.

After carefully analysing the data, it is interesting to find that an exponential relation exists between heat input and the hardness data measured for SAWP and pulsed deposited single beads. It is however noticed that at higher deposition rate (>1 m/min), i.e. heat input, there are regions where hardness maintained a constant values (as shown in Figure 4.7(b) for deposition at 1 m/min and 1.25 m/min). When further increasing the heat input, a large reduction in hardness was observed, which is due to large mixing of substrate material in the melt pool. The cross-sections show that the penetration depth is even higher than the bead height, as shown in Figure 4.4. In any case, it is interesting for future studies of the material response at high deposition speed using pulsed deposition to fully understand the causes.

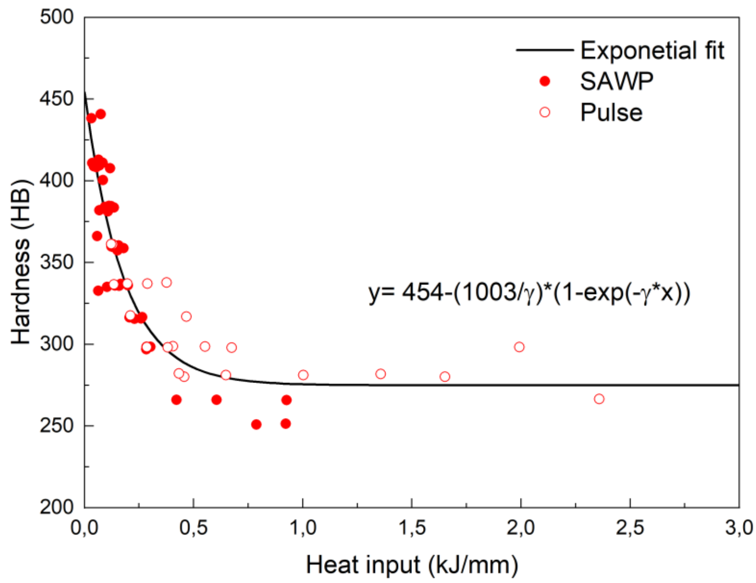

(a)

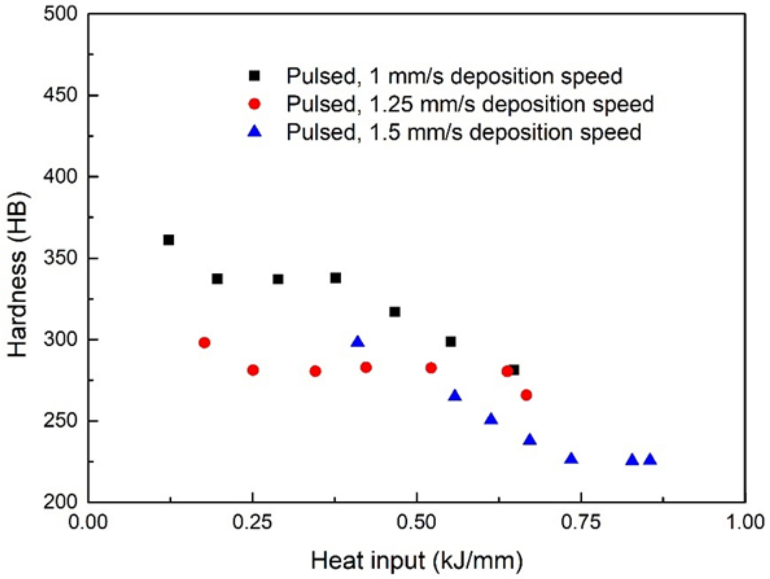

(b)

Figure 4.7 hardness distribution at different heat input; b) resulting hardness at high deposition speed using pulsed mode.

The exponential fit, presented in Figure 4.7(a), is represented by the Equation (6), corelating Brinell hardness (HB) with heat input (HI).

$$HB = 454 - \left(\frac{1003}{5.6}\right)\left(1 - e^{-5.6\,HI}\right) \tag{6}$$

This fitting shows fairly good agreement with the data, and the fitting parameter are shown in Table 4.1.

Table 4.1 Fitting parameters correlating Brinell hardness (HB) with heat input

Goodness Measures	
R^2	0.8677
aR^2	0.8625
P	0
SE	18.52
SSE	26060
F	166.2

AIC	688.3
BIC	695.4
DoF	76
AICc	688.6
Coefficients	
Y0	453.5026 ± 9.362
V0	1003.434 ± 144.6
K	5.589035 ± 0.6557
Equation	
y = 453.5026 - (1003.434 / 5.589035) * (1 - e^(-5.589035x))	

The measured strengths from the PIP device were then analysed and the data was plotted in Figure 4.8 and Figure 4.9. The fitting parameter are shown in the Table 4.2 and Table 4.3. For the yield strength (σ_Y[MPa]), the obtained fitted relationships are expressed in Equation (7).

$$\sigma_Y = 1130 - \left(\frac{2030}{3.6}\right)\left(1 - e^{-3.6\,HI}\right) \tag{7}$$

For ultimate tensile strength (σ_{UTS} [MPa]), the obtained relationships are expressed in Equation (8).

$$\sigma_{UTS} = 1354 - \left(\frac{2098}{3.9}\right)\left(1 - e^{-3.9\,HI}\right) \tag{8}$$

In all cases, the strength decreases rapidly until approximately 1 kJ/mm, suggesting that the material becomes less sensitive to further increases in heat input beyond this point. From these generalized equations, the denominators and exponents are identical values (e.g., 5.6 in Equation (6), 3.9 in Equation (7), and 3.6 in Equation (8)), which can be represented as γ in the following section..

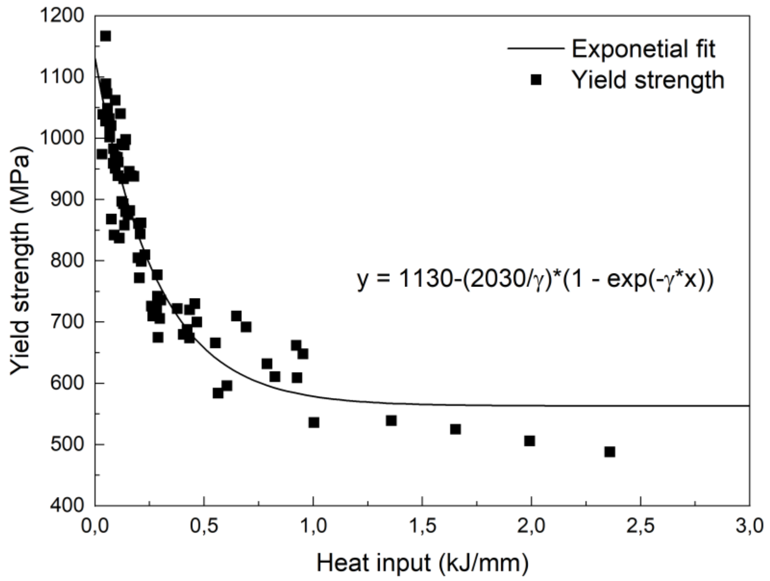

Figure 4.8 Yield strength distribution at different heat input

Table 4.2 Fitting parameters correlating yield strength (MPa) with heat input

Goodness Measures	
R^2	0.8891
aR^2	0.8843
P	0
SE	56
SSE	219500
F	187
AIC	797.8
BIC	804.7
DoF	70
AICc	798.2
Coefficients	
Y0	1130.417 ± 23.46
V0	2030.108 ± 265.8
K	3.580126 ± 0.4264
Equation	
y = 1130.417 - (2030.108 / 3.580126) * (1 - e^(-3.580126x))	

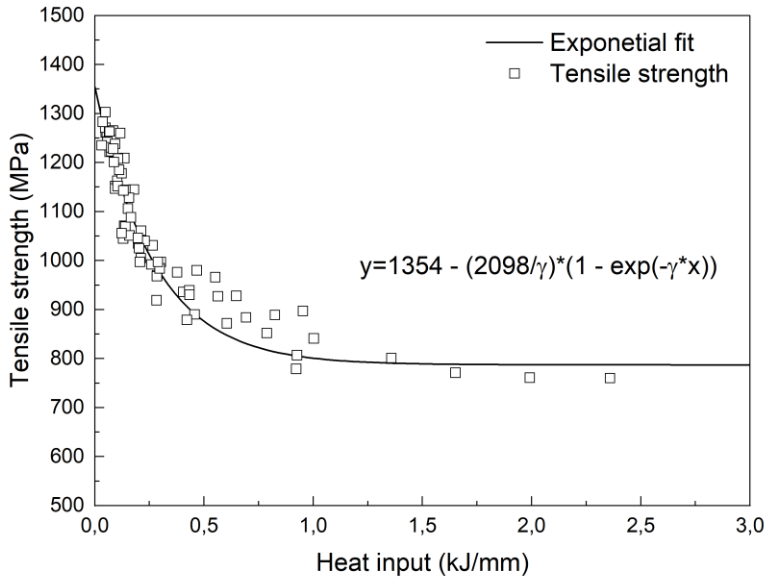

Figure 4.9 Ultimate tensile strength distribution at different heat input

Table 4.3 Fitting parameters correlating ultimate tensile strength (MPa) with heat input

Goodness Measures	
R^2	0.9216
aR^2	0.9183
P	0
SE	43.35
SSE	131500
F	274.4
AIC	760.4
BIC	767.3
DoF	70
AICc	760.8
Coefficients	
Y0	1353.812 ± 19.21
V0	2098.117 ± 230
K	3.924635 ± 0.3785
Equation	
y = 1353.812 - (2098.117 / 3.924635) * (1 - e^(-3.924635x))	

Comparing Vickers hardness and PIP device measured Brinell hardness

The sample extracted from a block produced at a low heat input of 0.2 kJ/mm was measured using the Vickers hardness tester and the PIP device is shown in Table 4.4. The tested sample is shown in Figure 4.10(a), in which the Brinell test locations are highlighted in red colour. Figure 4.10(b) shows the microstructure between different layers is shown. Brinell hardness was measured between the coarse and fine microstructure. The Vickers hardness was also measured at similar locations. A total of 15 Vickers hardness measurement were performed, and the results are shown in Table 4.4. After conversion of the Brinell hardness to Vickers hardness based on ISO 18265-2003 [59], the measurements show good agreement. This means that the PIP can provide reliable hardness measurements.

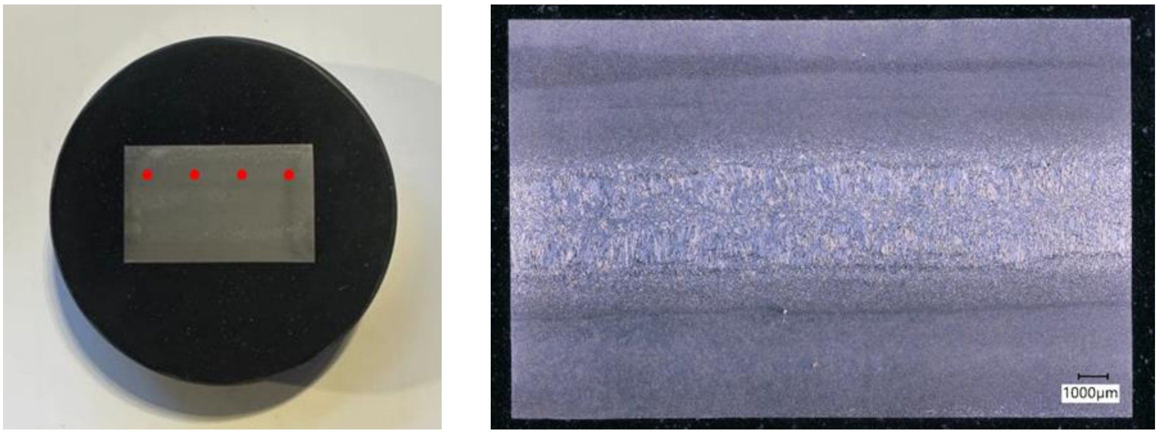

(a) (b)

Figure 4.10 (a) locations where the Brinell hardness was tested (b) cross-section of the tested sample.

Table 4.4 Comparing Vickers hardness and Brinell hardness

Test number	Vickers Hardness (HV10)	Brinell hardness (HB)	Vickers hardness converted from Brinell hardness (HV10)
1		158	167
2		171	180
3		158	167
4		160	168
Average	175 ± 2.6	162 ± 6.2	171 ± 6.4

Converting the Brinell hardness to Vickers hardness and comparing it in Figure 4.11 shows some marginal differences between them, but they are still in a good agreement. Therefore, the yield strength can be computed using equations (9) [60].

$$\sigma_Y = -90.7 + 2.876\ HV \tag{9}$$

The results are shown in Figure 4.12(a). The ultimate tensile strength can be computed using Equation (10) [60].

$$\sigma_{UTS} = -99.8 + 3.734\ HV \tag{10}$$

The results shown in Figure 4.12(a). It is interesting to note that the PIP-measured yield strength to be low compared to the computed yield strength, while the ultimate tensile strengths are in good agreement. The low yield strength measured may be due to the fact that the FEM input parameters (Young's modulus and Poisson's ratio) [61] used in the PIP device are based on data collected from forged and cast materials, which can be different from the WAAM-deposited material [62, 63]. The ultimate tensile strength measurements agree well with the computed values.

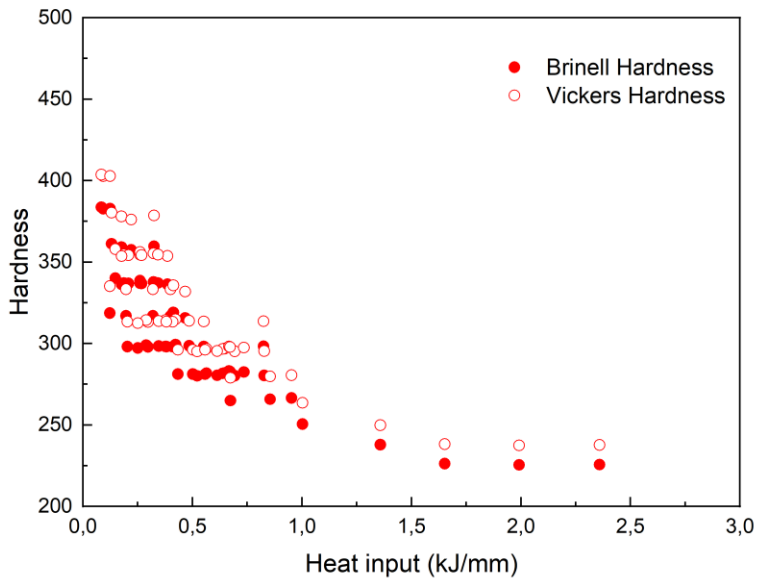

Figure 4.11 Comparison of Brinell hardness and Vickers hardness

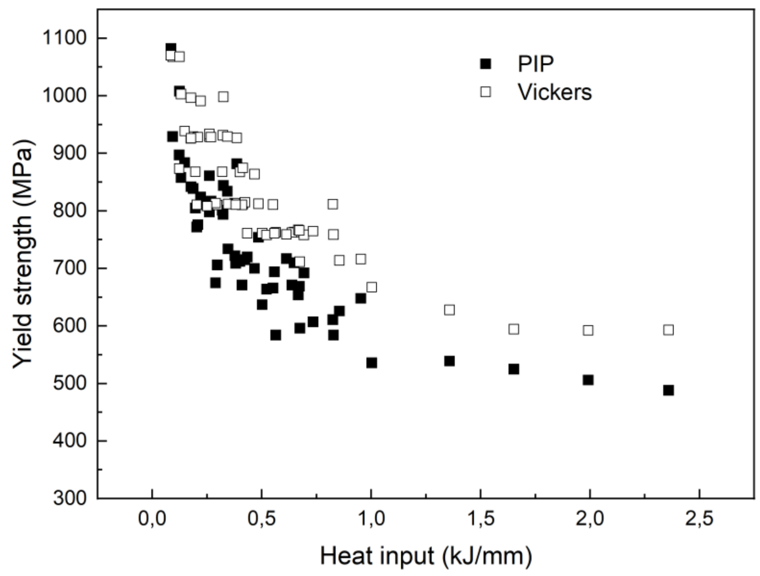

(a)

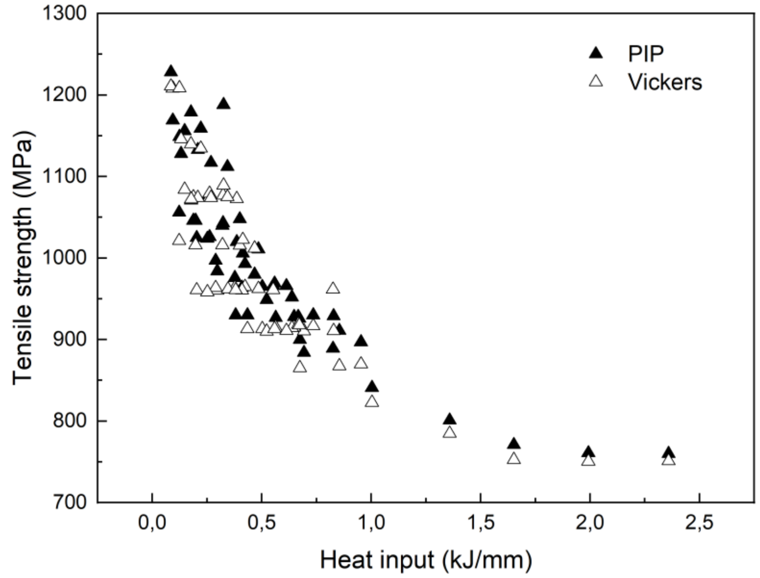

(b)

Figure 4.12 Comparison of the measured strength using PIP and the computed strength (a) yield strength (b) ultimate tensile strength

4.3 PIP Measurement on the Bead Deposited on the Substrate with Different Preheating Temperatures

As material properties are determined by its microstructure, which results from the cooling condition during solidification process, simple experiments were carried out to have a better understanding of the material's response when deposition occurs on the substrate with different starting temperatures. This can provide data for future research and for the optimisation that is running parallel in another project. Single beads were deposited using a heat input of 0.37 kJ/mm on the 10 mm substrate with different pre-heating temperatures of 25 °C, 50 °C, 100 °C and 200 °C, respectively. The deposited beads were cross-sectioned and prepared for PIP measurements. The measured Brinell hardness values are shown in Figure 4.13(a). Figure 4.13(a) shows that with increased substrate temperature, the hardness gradually decreases. The reduction in hardness with increasing pre-heating temperatures is due to the mixing of the substrate and the deposited material, as observed earlier in Figure 4.7(b). In terms of effective heat input, preheating the substrate introduces additional external heat to the weld area. This extra heat effectively increases the total thermal energy available for the melting, similar to increasing the welding heat input. This allows the process to penetrate deeper into the substrate while simultaneously reducing the bead height and widening the weld pool, as shown in Figure 4.13(b). The increased substrate temperature will promote penetration depth. In the 3D deposition process, these experiments help to define the interpass temperature, which avoids excessive penetration that can cause geometrical issues and pose the risk of reduced material mechanical properties. The effect of substrate temperature to the yield and tensile strength is shown in Figure 4.14.

Comparing the PIP measured hardness or strength to the empirical relation obtained and shown in Figure 4.7(a), Figure 4.8, and Figure 4.9, it appears that there may be a relation between the generalized equation (6), (7), and (8) in which the measured upper limit is constrained by the material's highest hardness or strength (C_{max}), and measured lower limits is constrained by the material's lowest properties (C_{min}), and the exponent (γ) may be related to the cooling rate, as the resulting mechanical properties of the deposited material are determined by the resulting grain size and orientation, which are determined by the cooling rate. Hence, the exponential relation found can be generalised and described in Equation (11).

$$y = C_{max} - C_{min}(1 - e^{-\gamma * x}) \tag{11}$$

where C is the material properties, γ is defined as a parameter related to the process and x is heat input. It will be interesting for future investigation of the exact correlation with systematic experiment design and finite element simulations. This is beyond the scope of the current study. However, this empirical relation will be used for analysing in the following sections.

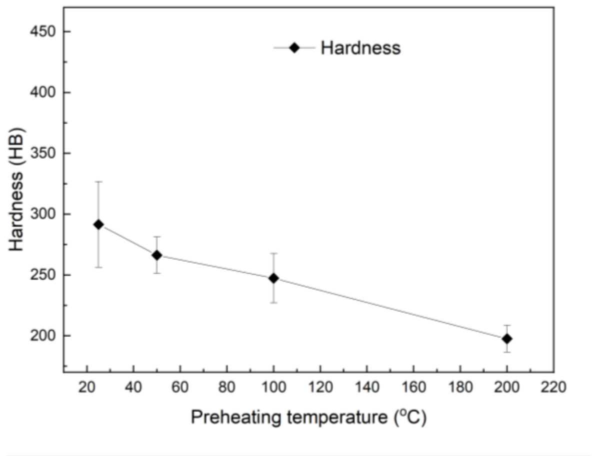

(a)

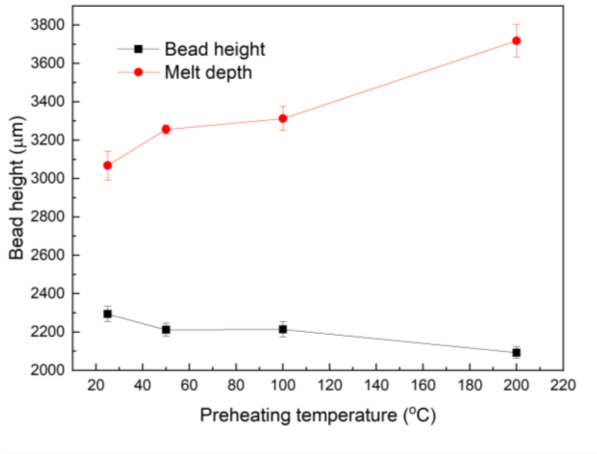

(b)

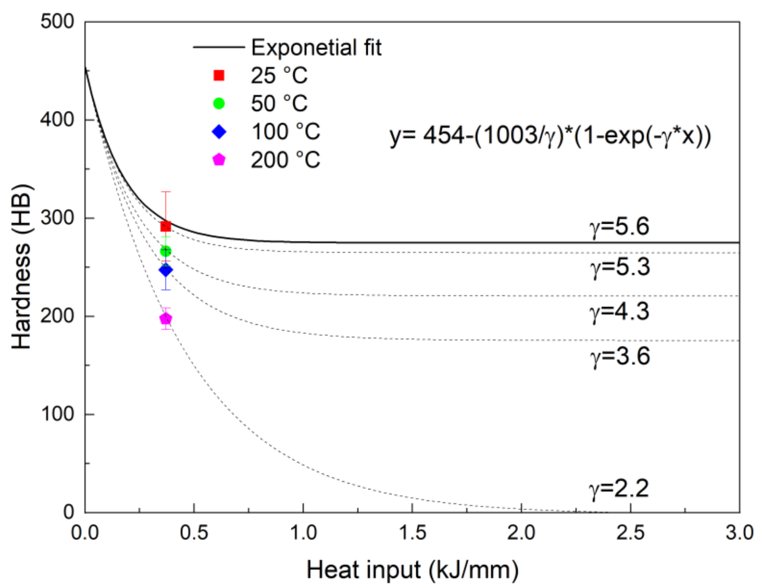

(c)

Figure 4.13 (a) Hardness reduction as substrate temperature increases, (b) the variation of bead height and melt depth at different substrate temperatures, (c) comparing hardness at different substrate temperatures.

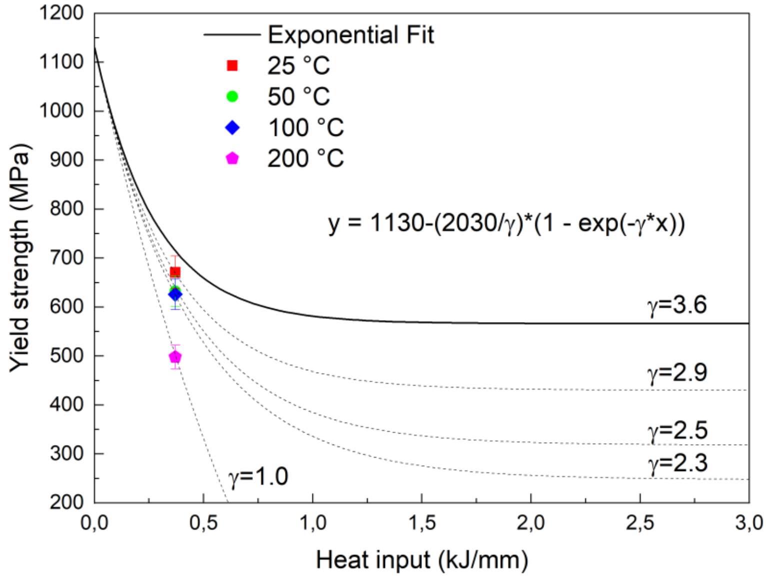

(a)

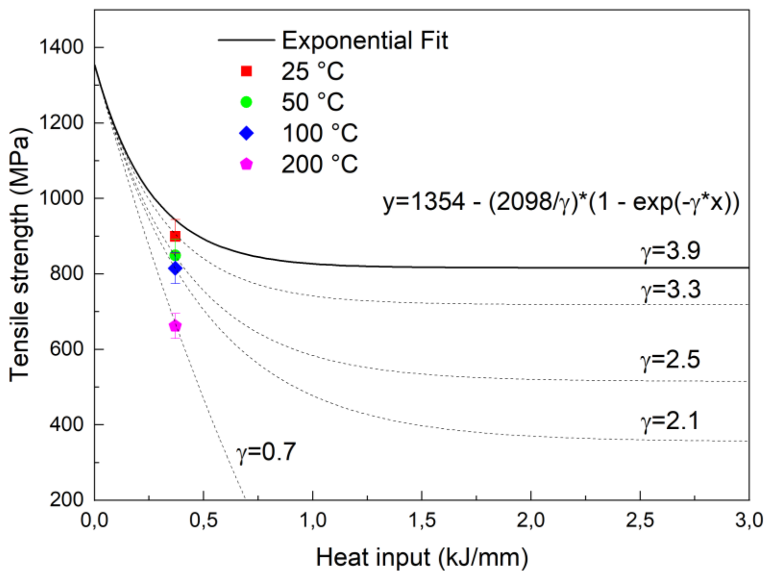

(b)

Figure 4.14 (a) empirical relation of the yield strength at different substrate temperatures, (b) empirical relation of the tensile strength at different substrate temperature.

4.4 Mechanical Properties Measurements of the As-Deposit 3D Block

Prior to this study, an parallel project was carried out in the traditional approach by depositing the 3D block using selected condition for material property evaluation. Three different heat inputs were selected to investigate the material's response, and the selected conditions is presented in Table 3.5. The mechanical properties, such as hardness, tensile strength, and yield strength, of the 3D block deposit are expected to be influenced by the microstructural evolution that occurs during the multilayer deposition process. As illustrated in Figure 4.15, a cross-section of single bead deposits on the substrate steel shows the initial microstructure before any overlapping occurs. Two primary grain structures are observed: columnar and equiaxed. Columnar grains generally form near the fusion line due to the initial rapid cooling associated with the large temperature gradient between the molten metal and the surrounding solidified material. As solidification progresses, the release of latent heat from the solidifying metal reduces the cooling rate. This slower and more directional cooling promotes the growth of elongated, column-like grains that develop perpendicular to the fusion line. In contrast, equiaxed grains typically form farther away from the fusion line, where the cooling rate increases. In these areas, the temperature difference between the molten metal and the surrounding solid material is less influenced by latent heat, allowing for more rapid and uniform cooling. This faster cooling promotes the development of smaller, randomly oriented grains with nearly equiaxed dimensions (similar in all directions).

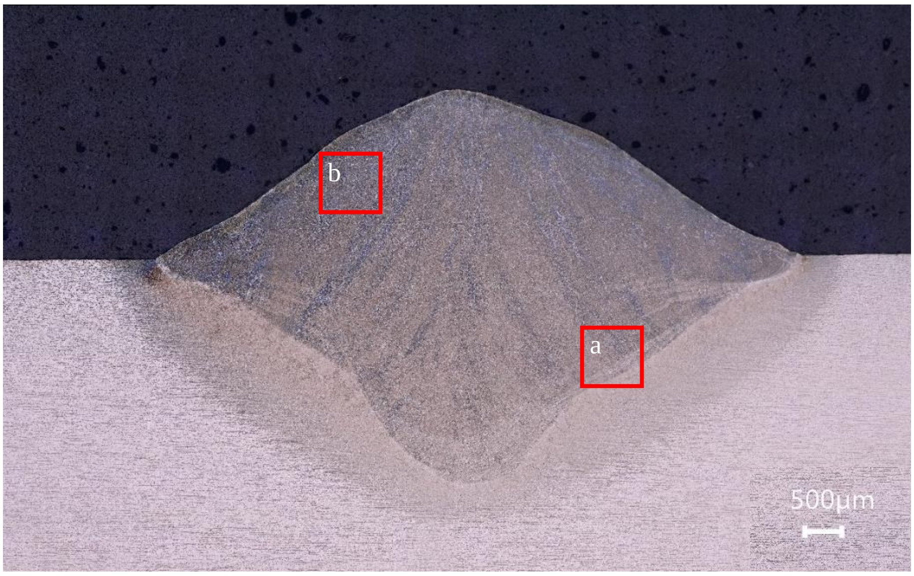

Figure 4.15 Microstructure of the WAAM-deposited single bead (a) columnar grains (b) equiaxed grains

Following the single bead analysis, the focus shifts to the 3D WAAM-deposited block, where repeated thermal cycles from multilayer deposition alter the grain structure significantly compared to single bead deposits. The microstructure of the 3D WAAM-deposited block was analysed with a focus on two distinct regions: near the top and close to the substrate, as illustrated in Figure 4.16. The microstructure of the top region is presented in Figure 4.17 (a), (c), (e), while the microstructure of the bottom region is shown in Figure 4.17 (b), (d), (f). Consistent with observations from single-bead tests, both regions predominantly feature columnar grains. However, in the block, these columnar grains are coarser, likely due to grain growth caused by the heat from the addition of new material in subsequent layers as they cool.

The grain size and characteristics vary from the lower to upper sections of the block due to differences in thermal histories compared to single beads as a result of repeated heating and cooling cycles during multilayer deposition. In the experiments conducted, this trend is consistent across the three ranges of heat input. At the very top of the block, a transition to more refined, equiaxed grains occurs because the layers in the upper regions experience less reheating compared to the lower regions. This reduced reheating limits the growth of columnar grains and promotes a more uniform grain size distribution. In contrast, the region near the substrate exhibits a coarser grain structure.

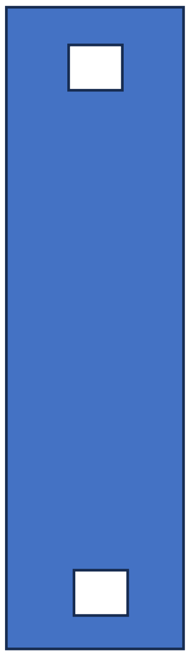

Figure 4.16 Schematic showing the location of the microstructure observations

Top Region Bottom Region

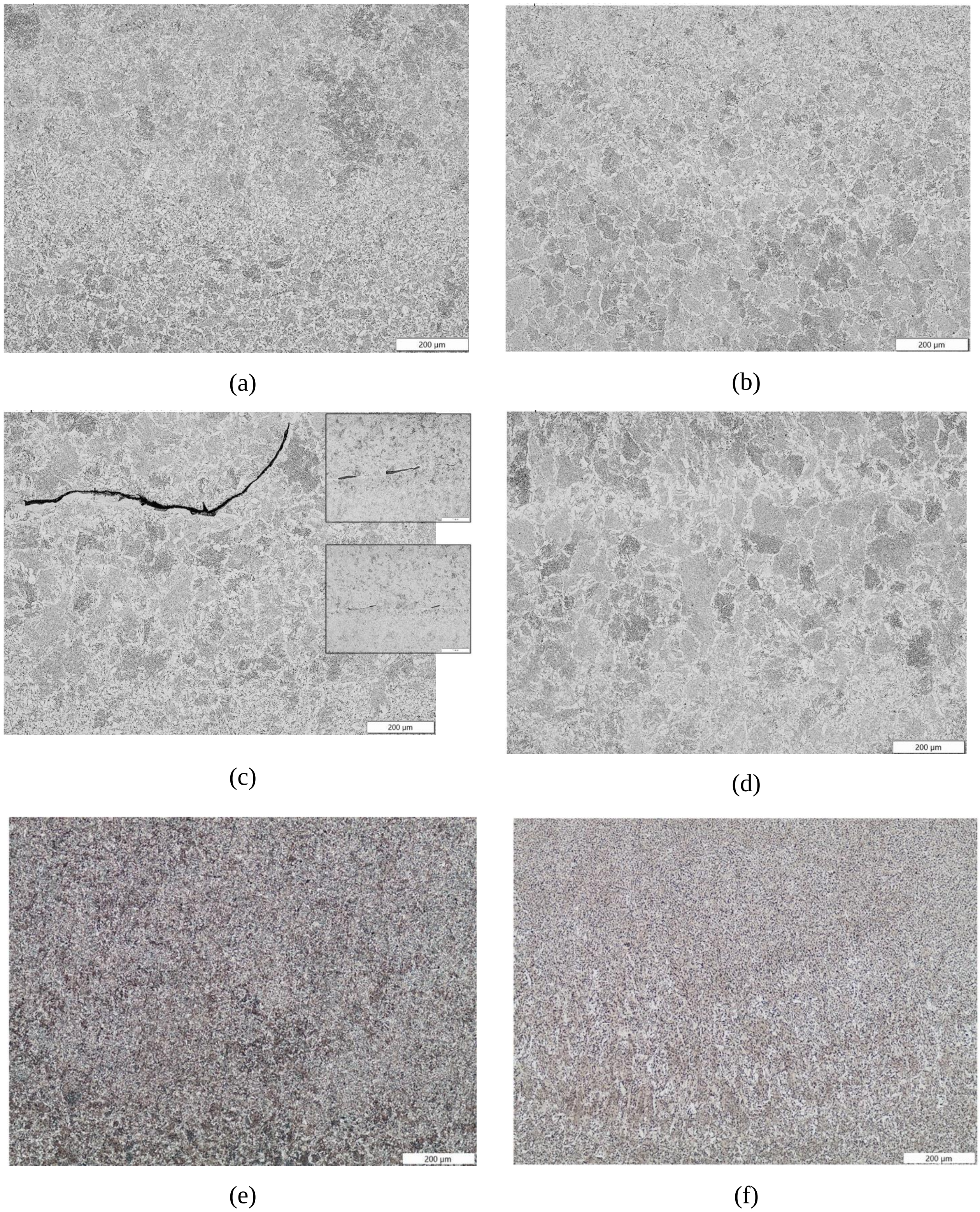

Figure 4.17 Microstructure of the WAAM-deposited block at different heat input ranges : (a-b) 0.216 kJ/mm, (c-d) 0.666 kJ/mm, and (e-f) 1.067 kJ/mm.

Table 4.5 presents the average hardness of a block deposit in the upper and lower regions for different levels of heat input. At low heat input, both regions exhibit the highest hardness, with values of 225.2±7.3 HB in the upper region and 217.1±8.2 HB in the lower region, indicating a slight harder material structure. As the heat input increases to medium, the hardness in the upper region decreases to 207.6±9.9 HB, while the lower region shows 212.8±9.7 HB, indicating limited difference between the regions and greater variability in the hardness measurements. At high heat input, the upper region measures 196±2.7 HB and the lower region measures 175±2.6 HB, reflecting a softer material structure. Overall, the trend shows that as the heat input increases, the hardness of the material decreases, particularly in the lower region. The expected higher hardness in the upper region at medium heat input is not as pronounced, possibly due to localized microstructural defects, such as cracks, as shown in Figure 4.17(c), which can reduce hardness by introducing weak points within the material's microstructure.

Table 4.5 Average hardness for different heat input ranges

Heat Input	Upper Region	Lower Region
Low	225.2±7.3 HB	217.1±8.2 HB
Medium	207.6±9.9 HB	212.8±9.7 HB
High	196±2.7 HB	175±2.6 HB

Table 4.6 presents the tensile properties of a welded material at different heat inputs, measured in the horizontal, vertical, and transverse directions. The data reflects the average results of samples tested in each direction. As shown in the table, samples welded with low heat input demonstrated higher tensile strengths (both Ultimate Tensile Strength (UTS) and 0.2% Yield Strength (YS)) across all directions compared to those with medium and high heat inputs. However, these samples exhibited lower elongation percentages. In contrast, samples with high heat input showed the lowest tensile strengths but the highest elongation values.

Notably, the variation in tensile properties between the horizontal, vertical, and transverse directions is relatively minor for each heat input level. This indicates that the mechanical properties are more significantly influenced by the heat input rather than the direction of testing. It is also observed that the increase in heat input leads to a trade-off between strength and ductility, while strength (UTS and YS) decreases, ductility (elongation) increases.

Table 4.6 The tensile result of the sample tested along different direction

Heat Input	Direction	UTS (MPa)	0.2 % YS (MPa)	Elongation (%)
Low	Horizontal	679.5	624	24
	Vertical	681.5	625	22.5
	Transverse	683	623	22.75
Medium	Horizontal	657.5	584	21.5
	Vertical	654.5	567	23.5
	Transverse	658.5	577.5	20.5
High	Horizontal	570	475	26.95
	Vertical	559	452	29.7
	Transverse	562	476	27.2

The observation is consistent with the Hall-Petch effect, which states that as grain size decreases (typically with lower heat input and faster cooling rates), the material hardness and strength increase [64]. Overall, as the heat input increases, the hardness decreases, particularly in the lower region, aligning with the Hall-Petch relationship. As the primary focus of this study is on the data analysis of process conditions to correlate single bead with 3D block deposition and establish a methodology to guide optimisation, the examination of microstructure material serves only to support the methodology and is not discussed in detail.

4.5 Comparison of As-Deposited 3D Block Experimental Results with the Empirical Relationship

The obtained results from the 3D block deposit in Table 3.5 were compared with the empirical relation (the exponential fit) obtained in this study. The comparisons are plotted in Figure 4.18. For reference, deposition conditions of the 3D blocks and the obtained exponent (γ) from the empirical relationship are shown in Table 4.7 and Table 4.8 respectively.

Table 4.7 Deposition condition of the 3D block deposit

Block test name	Heat Input (kJ/mm)	Transfer mode	Dimension (T x L x H)	Program-med Layer	Interlayer Temperature (°C)	Interpass Temperature (°C)	Cooling time each layer (minutes)	Voltage (V)	Current (A)	Travel Speed (m/min)	Crater Voltage (V)	Crater Current (A)	Crater Time (s)
TP 17	0.216	S-AWP	90 x 300 x 250	114	120	-	0	18	175	0.7	10	175	0
TP 19	0.666	Pulse	90 x 300 x 250	98	-	80	11	32.7	335	0.79	26.6	150	0.3
TP 12	1.067	Pulse	90 x 250 x 250	84	-	125	0	32.7	340	0.5	24.7	150	2

Table 4.8 Summary of exponent (γ) values obtained

Condition	Hardness	Yield strength	Tensile strength	Substrate dimension (mm^3)
Single bead ramping	5.6	3.6	3.9	300 × 200 × 30
25 °C	5.3	2.9	3.3	250 × 60 × 10
50°C	4.3	2.5	2.5	
100°C	3.6	2.3	2.1	
200°C	2.2	1	0.7	

When deposition was performed at an interpass temperature of 80 °C and 125 °C, it can be seen together with the Figure 4.13, it appears that blocks TP19 and TP12 both agree well with single bead test that were measured at a substrate temperature of 100 °C mentioned in previous chapter. The sensor used for temperature control can have ± 20 °C variation depending on the surface condition, therefore the hardness of TP19 and TP12 were expected to be as shown in the Figure 4.18(a). TP17 block was deposited at an interlayer temperature controlled at 120 °C with 14 overlapping beads. Figure 4.18(a), (b) and (c) all suggested that the actual deposition temperature of the material is higher than 200 °C. For the yield and tensile strengths as shown in Figure 4.18 (b) and Figure 4.18(c), it is shown that the deposition was done at temperatures below 100 °C. The tensile values were fairly close to what was expected, while the deviation of the yield strength values may be due to the large scatter observed in the PIP measurement. This scatter may be attributed to inaccurate indentation locations, which could result from difficulties in aiming the indenter precisely on the material surface, as well as the assumed limitations of the device that will be explained in the next section. This is not fully understood but could be interesting for further investigation in the future research work. Nevertheless, with further development of this approach, it is essential to establish a reliable and effective methodology for using PIP measurement to guide for 3D metallic printing and its process optimisations, which was one of the research questions that has been addressed now.

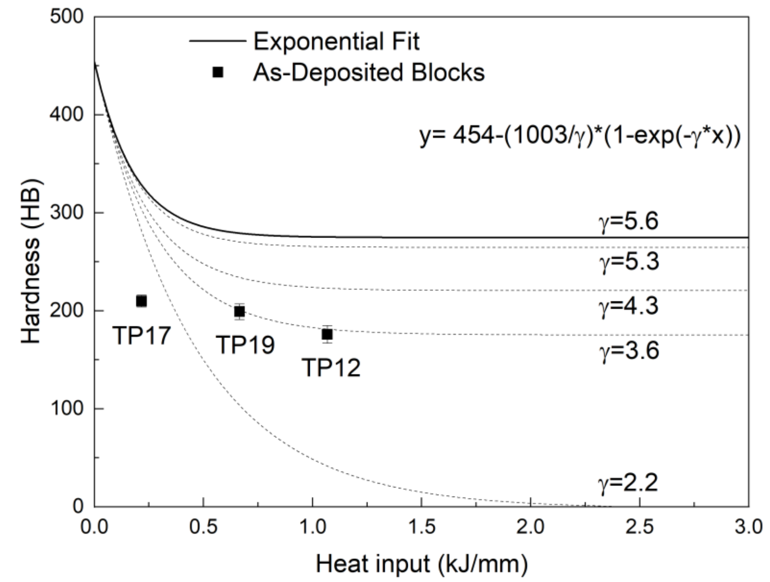

Exponential Fit
As-Deposited Blocks
y= 454-(1003/γ)*(1-exp(-γ*x))
γ=5.6
γ=5.3
γ=4.3
γ=3.6
γ=2.2
TP17
TP19
TP12
Hardness (HB)
Heat input (kJ/mm)
0
100
200
300
400
500
0.0
0.5
1.0
1.5
2.0
2.5
3.0

(a)

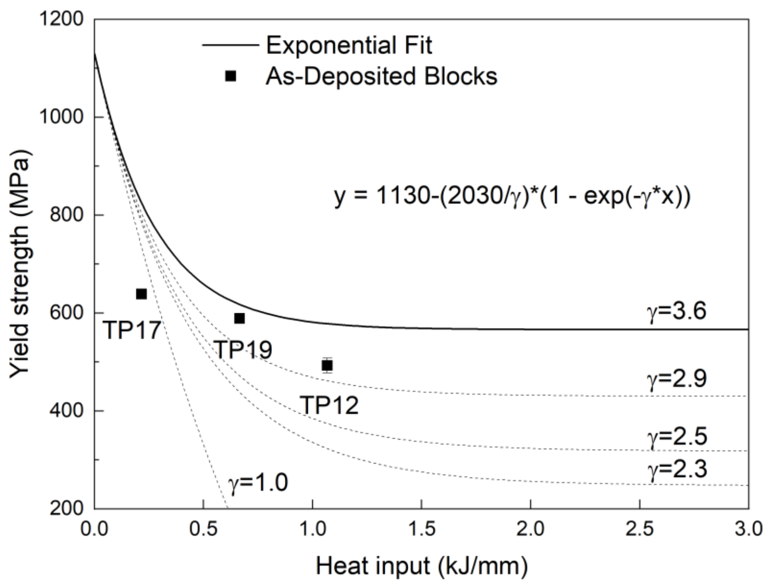

Exponential Fit
As-Deposited Blocks
y = 1130-(2030/γ)*(1 - exp(-γ*x))
γ=3.6
γ=2.9
γ=2.5
γ=2.3
γ=1.0
TP17
TP19
TP12
Yield strength (MPa)
Heat input (kJ/mm)
200
400
600
800
1000
1200
0.0
0.5
1.0
1.5
2.0
2.5
3.0

(b)

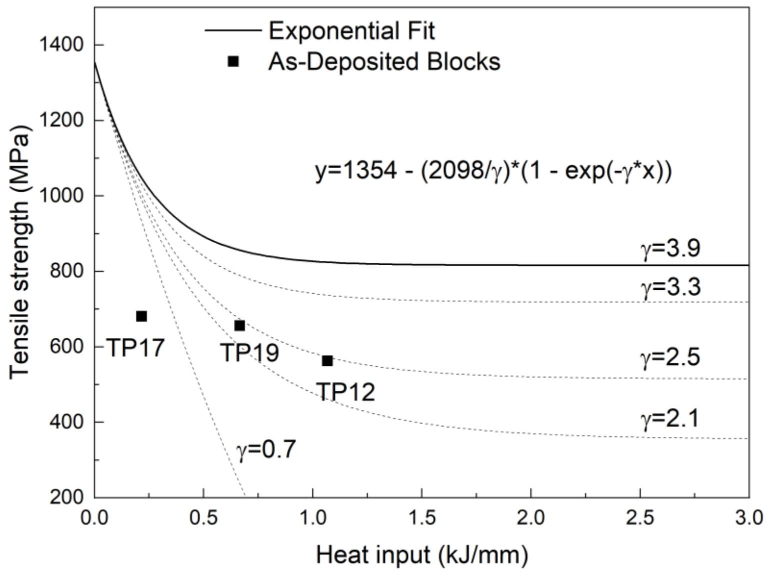

(c)

Figure 4.18 The comparison of 3D block deposit with the empirical relations, (a) hardness (b) yield strength (c) tensile strength

4.6 Limitation in the Yield Strength Value Between PIP and Uniaxial Testing

As a relatively novel technology, the PIP device is still under development and is regularly upgraded. During the experiment period of this project, repeated errors occurred in both hardware and software. Issues such as loose connections led to a broken indenter tip, while SEMPID errors resulted in incomplete measurements. These problems were promptly reported to the system provider for resolution as there is collaboration between the device manufacturer ans RAMLAB, the host company of this thesis. In addition, the latest license updates that the device underwent significantly reduced the frequency of errors compared to before, although errors are still encountered.

As the accurate elongation cannot be measured by the PIP, the elongation has not be analysed and disscused in this thesis. The relatively low yield strength measured in the PIP test, compared to the uniaxial test result, was initially attributed to Lüders band behaviour by the device manufacturer. Lüders band behaviour refers to localized regions of plastic deformation that appear after the yield point in the stress-strain curve, resulting in a stress plateau where the material undergoes plastic deformation with minimal stress increase [65]. This phenomenon is commonly observed in low-carbon steels, where interstitial carbon atoms hinder dislocation movement, delaying the onset of plastic deformation. When the material reaches its upper yield point, dislocations escape from these pinning carbon atoms, leading to a load drop and sudden burst in plastic deformation under constant load [66].

However, further investigation revealed that Lüders band behaviour was not the actual cause of the observed discrepancy. The challenges seem to come from the modelling approach used in the PIP system, particularly related to the factors inputted to simulate the back-calculation of material properties. The assumption of uniform elastic properties, specifically the Poisson's ratio used for all types of material, is not sufficient to accurately represent the actual material's response. In WAAM processes, the Poisson's ratio is relatively lower compared to other material processing methods [67], which may account for the poorer performance of WAAM-derived material properties relative to those from cast or forged materials. Currently, insufficient data is available to refine the model for additively manufactured (AM) materials specifically WAAM. To address this limitation, the developers are collaborating with companies in the additive manufacturing sector to collect the necessary data to improve the PIP model fitting. Despite these minor discrepancies, it remains possible to obtain trends that are useful for the further optimisation stage.

According to the device manufacturer’s latest update, an improved model fitting has been developed, which shifts the yield strength up by approximately 30-80 MPa and reduces the tensile strength by around 30-40 MPa as shown in Figure 4.19, which seems to be offer a beter measurement results, however considering the error bar, it is not fundamentally explain causes for lower yield strength measurements.

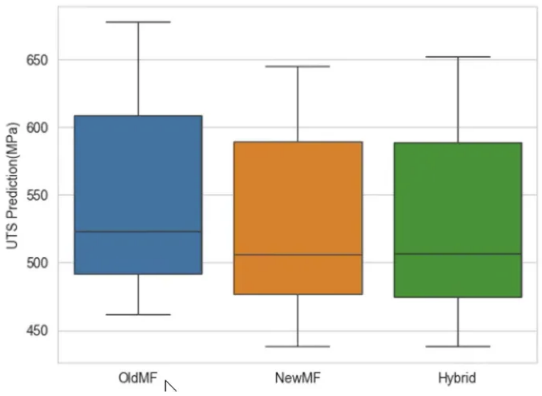

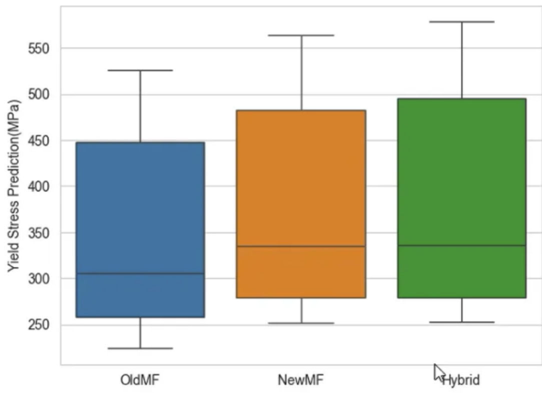

(a) (b)

Figure 4.19 Comparison of the old model fitting with the new model fitting (a) Tensile Strength (b) Yield Strength

The current lack of a certified and standardized testing procedure may also contribute to the observed scatter plotted in Figure 4.11 and Figure 4.12, where measurement were performed on the sample made at low heat input region. To further improve this and contribute to the standardisation of the measurement procedure using the PIP device, the mild steel, maraging steel, Inconel 718, Inconel 625, aluminium alloys, and steel alloys (potentially 17-4 PH stainless steel) were tested using the setting defined by the device manufacturer, which are popular materials interested and researched in the AM field.

The tests were executed without major issues according to the provided testing instruction, with no errors occurring in either software or hardware. However, it is important to note that certain issues, such as SEMPID errors and difficulties in detecting work hardening, still occurred during testing conducted under a standard setting, rather than the specific settings intended for the test. These factors may have contributed to the errors/imperfect results observed, which were not evident during the test. The operation experience will be valuable for future following up research. Hence, it is summarised in the following paragraph.

First, during the inter-lab test, the device required at least one hour of warm-up prior to testing. This warm-up requirement is not mentioned in the device user manual and was only communicated during an internal discussion with the provider, where they suggested that 20 minutes would be sufficient for stabilising all the electronics within the device.

Second, unlike the normal setting where displacement control is being used, load control was employed during the test. This was achieved by adjusting several inputs in the advanced settings, such as changing the ‘minimal indentation depth before achieving load point’ into 10 μm, ‘max work hardening parameter’ into 50.50, and ‘manual load point’ to the specified load for each material sample. In the load control method, a specific force is set as the target, while a displacement-controlled test is first run to determine the required load for sufficient indentation. Since the profilometer only requires the load value, the provider confirmed that both methods would yield the same desired load for the tests.

It is important to note that during displacement control, only the type of material input is needed to select the load for indenting based on the Young's modulus dataset. However, for steel and steel alloys, which are grouped together in the device, there is a wide range of load allowances. This could lead to differences in results compared to when the load is specifically determined in load control mode, which can be explored in more detail for further investigation in the future work. Additionally, the test was performed on additive manufactured material produced by a powder-based process, which may also contribute to the consistency of the testing results. Further in-depth research is still needed before applying PIP in Wire Arc Additive Manufacturing (WAAM) deposits, but the trends from the measurement results are sufficient for the data analysis in this thesis work.

5 Conclusion & Recommendation

The aim of this project is to explore how Profilometry-based Indentation Plastometry (PIP) can be applied to help provide a methodology to guide the process optimisation for scaling up (large) Wire Arc Additive Manufacturing (WAAM) deposits, focusing on the relationship between process parameters and mechanical properties. Through experimental testing and comprehensive data analysis, the correlation between these parameters has been evaluated and some conclusions can be drawn as follow.

- Both bead width and height increase with increased heat input, but penetration depth is more consistent across deposition speeds in SAWP mode. Pulsed mode deposition tends to result in deeper penetration.
- Increasing heat input leads to a reduction in hardness and strength due to slower cooling rates resulting larger grain.
- Increase substrate starting temperature reduce hardness promote the heat penetration.
- At high heat input, the hardness value can drop sharply due to larger mixing with substrate observed from the single bead ramping test, meaning that there will be a mixing ratio above which it can jeopardize the integrity of the deposited material. This will be less important for general 3D printing, but it will become import when 3D printing multi-material.
- The PIP Brinell hardness measurements agree well with the Vickers hardness measurements.
- The PIP yield strength measurements were lower compared to the uniaxial test result.
- The PIP ultimate tensile strength measured agree well with the uniaxial test results.

- The measurement scattering observed in the low heat input regions, it can be improved when standard measurement procedure is defined.
- The material properties of a 3D-deposited block are significantly influenced by microstructural evolution (repeated thermal cycles). Lower heat inputs yield higher hardness and strength, while higher heat inputs result in softer and weaker material structures.
- An exponential relationship between heat input and both hardness and strength was observed. The material becomes less sensitive to heat inputs beyond approximately 1 kJ/mm for the tested material in this thesis.
- This study made a successful attempt for applying the PIP measurement to corelate single bead material response (hardness and strengths) to the properties (hardness and strengths) of 3D block deposits using WAAM. The methodology can be effectively guides the parameter and procedure optimization.

The findings of this research provide a foundation for further research and refinement of the methodology. The following recommendations are proposed based on the observations:

- To refine the methodology, additional data at different heat inputs with different substrate starting temperatures are to be generated,
- A better sample design and improvements of the PIP measurement setup should be considered to improve the measurement accuracy and reduce scattering in low heat input regions, e.g. with overlapped beads, it can provide larger area for multiple measurements that is expected to reduce the measurement error
- The PIP fitting model should be refined to account for the unique properties of additively manufactured materials. Collaboration with additive manufacturing industries is recommended to collect sufficient data for improving the measurement accuracy of the PIP system.
- A comprehensive user guide and standard measurement procedure of the PIP device should be developed, which can offer more detailed instructions on handling operational errors and improving measurement precision.

Bibliography

[1] Dinovitzer M, Chen X, Laliberte J, et al. Effect of wire and arc additive manufacturing (WAAM) process parameters on bead geometry and microstructure. *Additive Manufacturing* 2019; 26: 138–146.

[2] Lee SH. Optimization of Cold Metal Transfer-Based Wire Arc Additive Manufacturing Processes Using Gaussian Process Regression. *Metals* 2020; 10: 461.

[3] Tomar B, Shiva S, Nath T. A review on wire arc additive manufacturing: Processing parameters, defects, quality improvement and recent advances. *Materials Today Communications* 2022; 31: 103739.

[4] Ziętala M, Durejko T, Polański M, et al. The microstructure, mechanical properties and corrosion resistance of 316L stainless steel fabricated using laser engineered net shaping. *Materials Science and Engineering: A* 2016; 677: 1–10.

[5] Sun L, Jiang F, Huang R, et al. Investigation on the process window with liner energy density for single-layer parts fabricated by wire and arc additive manufacturing. *Journal of Manufacturing Processes* 2020; 56: 898–907.

[6] Ya W. *Laser materials interactions during cladding: analyses on clad formation, thermal cycles, residual stress and defects*. University of Twente. Epub ahead of print 30 October 2015. DOI: 10.3990/1.9789491909313.

[7] Lin Z, Ya W, Subramanian VV, et al. Deposition of Stellite 6 alloy on steel substrates using wire and arc additive manufacturing. *Int J Adv Manuf Technol* 2020; 111: 411–426.

[8] Frazier WE. Metal Additive Manufacturing: A Review. *J of Materi Eng and Perform* 2014; 23: 1917–1928.

[9] Vafadar A, Guzzomi F, Rassau A, et al. Advances in Metal Additive Manufacturing: A Review of Common Processes, Industrial Applications, and Current Challenges. *Applied Sciences* 2021; 11: 1213.

[10] Ahn D-G. Directed Energy Deposition (DED) Process: State of the Art. *Int J of Precis Eng and Manuf-Green Tech* 2021; 8: 703–742.

[11] Shah A, Aliyev R, Zeidler H, et al. A Review of the Recent Developments and Challenges in Wire Arc Additive Manufacturing (WAAM) Process. *JMMP* 2023; 7: 97.

[12] Rajesh A. Anomaly Detection in WAAM Deposition of Nickel Alloys | TU Delft Repository, https://repository.tudelft.nl/record/uuid:49f88587-c44b-46a5-b363-3dc2b6f21865 (2023, accessed 20 July 2024).

[13] Sharifi SS, Fritsche S, Holzinger C, et al. Selection of Parameters for Optimized WAAM Structures for Civil Engineering Applications. *Materials* 2023; 16: 4862.

[14] Castillo Marasco E del. *Process optimization: a statistical approach*. New York: Springer, 2007.

[15] Liu Q, Wu H, Paul MJ, et al. Machine-learning assisted laser powder bed fusion process optimization for AlSi10Mg: New microstructure description indices and fracture mechanisms. *Acta Materialia* 2020; 201: 316–328.

[16] Karandikar J, Chaudhuri A, Smith S, et al. Process window estimation in manufacturing through Entropy-Sigma active learning. *Manufacturing Letters* 2022; 34: 87–92.

[17] Zavdoveev A, Pozniakov V, Baudin T, et al. Optimization of the Pulsed Arc Welding Parameters for Wire Arc Additive Manufacturing in Austenitic Steel Applications. Epub ahead of print 13 October 2021. DOI: 10.21203/rs.3.rs-964589/v1.

[18] Kumar A, Maji K, Shrivastava A. Investigations on Deposition Geometry and Mechanical Properties of Wire Arc Additive Manufactured Inconel 625. *Int J Precis Eng Manuf* 2023; 24: 1483–1500.

[19] Hussein NIS, Mohd Jmmani NAN, Ayof MN, et al. Simulation of wire and arc additive manufacturing of 308L stainless steel with cold arc gas metal arc welding. *JAEDS* 2021; 1: 88–96.

[20] Ding D, Pan Z, Cuiuri D, et al. A practical path planning methodology for wire and arc additive manufacturing of thin-walled structures. *Robotics and Computer-Integrated Manufacturing* 2015; 34: 8–19.

[21] Ps G, S J, Dt S. Influence of heat input on microstructure and mechanical behaviour of austenitic stainless steel 316L processed in wire and arc additive manufacturing. *Proceedings of the Institution of Mechanical Engineers, Part E: Journal of Process Mechanical Engineering* 2023; 237: 149–161.

[22] Wang Z, Zimmer-Chevret S, Léonard F, et al. Improvement strategy for the geometric accuracy of bead's beginning and end parts in wire-arc additive manufacturing (WAAM). *Int J Adv Manuf Technol* 2022; 118: 2139–2151.

[23] device.report. CAMPBELL HAUSFELD WS099001 Shielded Metal Arc Welder Instruction Manual. *device.report*, https://device.report/manual/6417506 (accessed 18 September 2024).

[24] Jiang F, Sun L, Huang R, et al. Effects of Heat Input on Morphology of Thin-Wall Components Fabricated by Wire and Arc Additive Manufacturing. *Adv Eng Mater* 2021; 23: 2001443.

[25] Jin W, Zhang C, Jin S, et al. Wire Arc Additive Manufacturing of Stainless Steels: A Review. *Applied Sciences* 2020; 10: 1563.

[26] Babu A, Ebrahimi A, Wu K-H, et al. Local control of microstructure and mechanical properties of high-strength steel in electric arc-based additive manufacturing. *Journal of Materials Research and Technology* 2023; 26: 1508–1526.

[27] Pattanayak S, Sahoo SK. Gas metal arc welding based additive manufacturing—a review. *CIRP Journal of Manufacturing Science and Technology* 2021; 33: 398–442.

[28] Gudur S, Nagallapati V, Pawar S, et al. A study on the effect of substrate heating and cooling on bead geometry in wire arc additive manufacturing and its correlation with cooling rate. *Materials Today: Proceedings* 2021; 41: 431–436.

[29] Bang K-S, Jung D-H, Park C, et al. Effects of welding parameters on tensile strength of weld metal in flux cored arc welding. *Science and Technology of Welding and Joining* 2008; 13: 509–514.

[30] Liu H, Feng T, Chen C, et al. Study on the Relationship between Process Parameters and theFormation of GTAW Additive Manufacturing of TC4 Titanium Alloy Using the Response Surface Method. *Coatings* 2023; 13: 1578.

[31] Wei Z, Laizhu J, Jincheng H, et al. Study of mechanical and corrosion properties of a Fe–21.4Cr–6Mn–1.5Ni–0.24N–0.6Mo duplex stainless steel. *Materials Science and Engineering: A* 2008; 497: 501–504.

[32] Le VT, Mai DS, Doan TK, et al. Wire and arc additive manufacturing of 308L stainless steel components: Optimization of processing parameters and material properties. *Engineering Science and Technology, an International Journal* 2021; 24: 1015–1026.

[33] Constant Current vs Constant Voltage Output, https://www.lincolnelectric.com/hr-HR/Welding-and-Cutting-Resource-Center/Process-and-Theory/Constant-Current-vs-Constant-Voltage-Output (accessed 19 September 2024).

[34] Zhao Y, Chung H. Influence of power source dynamics on metal and heat transfer behaviors in pulsed gas metal arc welding. *International Journal of Heat and Mass Transfer* 2018; 121: 887–899.

[35] Wu Y, Li Z, Wang Y, et al. Study on the Process Window in Wire Arc Additive Manufacturing of a High Relative Density Aluminum Alloy. *Metals* 2024; 14: 330.

[36] Amps & Volts, https://app.aws.org/forum/topic_show.pl?tid=29334 (accessed 19 September 2024).

[37] Panchenko O, Kurushkin D, Isupov F, et al. Gas Metal Arc Welding Modes in Wire Arc Additive Manufacturing of Ti-6Al-4V. *Materials* 2021; 14: 2457.

[38] Prado-Cerqueira JL, Camacho AM, Diéguez JL, et al. Analysis of Favorable Process Conditions for the Manufacturing of Thin-Wall Pieces of Mild Steel Obtained by Wire and Arc Additive Manufacturing (WAAM). *Materials* 2018; 11: 1449.

[39] Koppu AK, Lautre NK, Motwani A, et al. Mechanical and Microstructure Investigation of TiC-inoculated SS316LSi Thin Wall Deposited by CMT-WAAM. *Trans Indian Inst Met* 2023; 76: 2307–2314.

[40] Fronius CMT and Panasonic SAW-P: Short-circuit transfer compared, https://www.ramlab.com/resources/cmt-and-saw-p-a-comparison/ (accessed 9 September 2024).

[41] Welding Transfer Modes: Spray, Global & Short Circuiting. *Weld Guru*, https://weldguru.com/welding-transfer-modes/ (2022, accessed 18 October 2024).

[42] Clyne TW, Campbell JE, Burley M, et al. Profilometry-Based Inverse Finite Element Method Indentation Plastometry. *Adv Eng Mater* 2021; 23: 2100437.

[43] Dean J, Clyne TW. Extraction of plasticity parameters from a single test using a spherical indenter and FEM modelling. *Mechanics of Materials* 2017; 105: 112–122.

[44] Balavar M, Mirzadeh H. Controlling the mechanical properties of carbon steel by thermomechanical treatment. Kish Island, Iran, p. 020038.

[45] Maleki M, Mirzadeh H, Zamani M. Effect of Intercritical Annealing on Mechanical Properties and Work-Hardening Response of High Formability Dual Phase Steel. *steel research int* 2018; 89: 1700412.

[46] Mohsenzadeh MS. improvement of tensile properties of low-carbon steels via short-time intercritical annealing. *Acta Metall Slovaca* 2023; 29: 17–21.

[47] Introduction to Indentation Plastometry. *Plastometrex*, https://plastometrex.com/blogs/introduction-to-indentation-plastometry (accessed 20 July 2024).

[48] Gu W, Campbell J, Tang Y, et al. Indentation Plastometry of Welds. *Adv Eng Mater* 2022; 24: 2101645.

[49] Tang Y, Campbell J, Burley M, et al. Profilometry-based indentation plastometry to obtain stress-strain curves from anisotropic superalloy components made by additive manufacturing. *Materialia* 2021; 15: 101017.

[50] Southern T, Campbell JE, Kourousis KI, et al. Indentation Plastometry for Study of Anisotropy and Inhomogeneity in Maraging Steel Produced by Laser Powder Bed Fusion. *steel research int* 2023; 94: 2200881.

[51] Lancaster RJ, Barnard NC, Haigh B, et al. Evaluating the efficacy of alternative small scale test methodologies in deriving the mechanical properties of additive manufactured materials. *Journal of Materials Research and Technology* 2023; 26: 9328–9345.

[52] Satiti BE. *Indentation Plastometry for optimization of WAAM deposit*. External Reseach Project Report, Rotterdam: Ramlab BV, February 2024.

[53] Klusák J, Horník V, Lesiuk G, et al. Comparison of high- and low-frequency fatigue properties of structural steels S355J0 and S355J2. *Fatigue Fract Eng Mat Struct* 2021; 44: 3202–3213.

[54] Smismans T, Chernovol N, Lauwers B, et al. Influence of post-heat treatments on fatigue response of low-alloyed carbon-manganese steel material manufactured by Direct Energy Deposition-Arc technique. *Materials Letters* 2021; 302: 130465.

[55] Ya W, Pathiraj B, Liu S. 2D modelling of clad geometry and resulting thermal cycles during laser cladding. *Journal of Materials Processing Technology* 2016; 230: 217–232.

[56] Lin Z. *Wire and Arc Additive Manufacturing of Thin Structures Using Metal-Cored Wire Consumables Microstructure, mechanical properties, and experiment-based thermal model*. Delft University of Technology, https://repository.tudelft.nl/record/uuid:ed3515f3-b43a-4cdc-9f11-2e249c97bbed (2019).

[57] Ventrella VA, Berretta JR, De Rossi W. Pulsed Nd:YAG laser seam welding of AISI 316L stainless steel thin foils. *Journal of Materials Processing Technology* 2010; 210: 1838–1843.

[58] Evans GM. Factors affecting the microstructure and properties of C-Mn all-weld-metal deposits. Epub ahead of print 2015. DOI: 10.13140/RG.2.1.1631.8882.

[59] International Organization for Standardization (ISO). *Metallic materials — Conversion of hardness values*. International Standard ISO 18265:2013, Geneva, Switzerland: International Organization for Standardization (ISO), 1 October 2013.

[60] Pavlina EJ, Van Tyne CJ. Correlation of Yield Strength and Tensile Strength with Hardness for Steels. *J of Materi Eng and Perform* 2008; 17: 888–893.

[61] Campbell JE, Zhang H, Burley M, et al. A Critical Appraisal of the Instrumented Indentation Technique and Profilometry-Based Inverse Finite Element Method Indentation Plastometry for Obtaining Stress–Strain Curves. *Adv Eng Mater* 2021; 23: 2001496.

[62] Sword JI, Galloway A, Toumpis A. An environmental impact comparison between wire + arc additive manufacture and forging for the production of a titanium component. *Sustainable Materials and Technologies* 2023; 36: e00600.

[63] Tian G, Wang X, Wang W, et al. Microstructure, Mechanical Properties, and Galvanic Corrosion of 10CrNi3MoV Fabricated by Wire Arc Additive Manufacturing. *Metals* 2021; 11: 1235.

[64] Purtscher PT, Cheng Y-W. *Structure-property relationships in microalloyed ferrite-earlite steels- phase 1 : literature review, research plan, and initial results*. 0 ed. NIST IR 3992, Gaithersburg, MD: National Institute of Standards and Technology.

[65] Zhang M, Li R, Ding J, et al. In situ high-energy X-ray diffraction mapping of Lüders band propagation in medium-Mn transformation-induced plasticity steels. *Materials Research Letters* 2018; 6: 662–667.

[66] Lüders band behaviour, http://6034553.hs-sites.com/knowledge/lüders-band-behaviour (accessed 23 October 2024).

[67] Huang C, Kyvelou P, Zhang R, et al. Mechanical testing and microstructural analysis of wire arc additively manufactured steels. *Materials & Design* 2022; 216: 110544.

Appendix A

This appendix presents cross-sectional micrographs of the samples analysed throughout this thesis, arranged by increasing heat input. A total of 119 samples were examined, covering both Pulsed and Super Active Wire Process (SAWP) modes. To facilitate differentiation, samples in Pulsed mode are denoted with bold and underlined numbering.

1 2 3 4 5

6 7 8 9 10

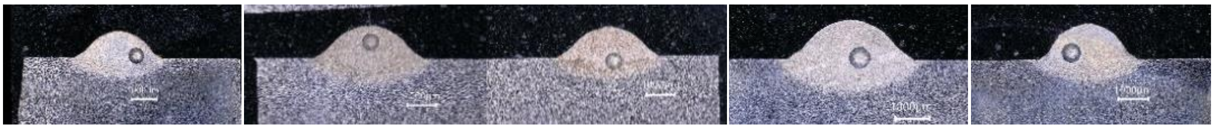

11 12 13 14 15

16 17 18 19 20

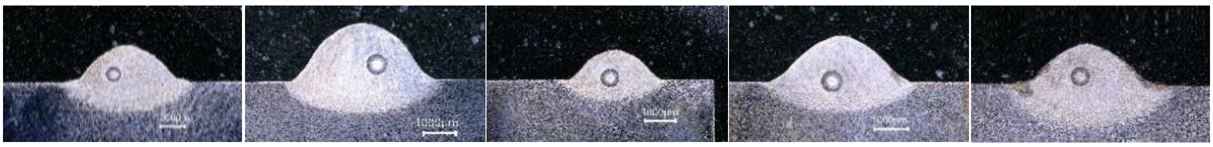

21 22 23 24 **25**

26 27 28 29 30


31

32

33
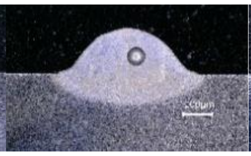
34

35

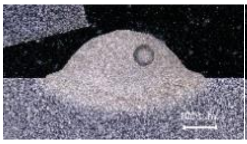
36

37
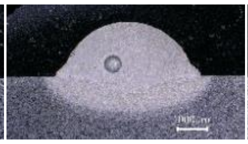
38
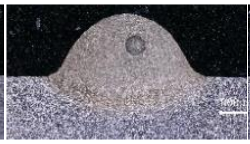
39

40


41
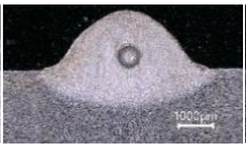
42
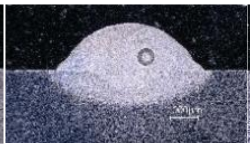
43

44

45

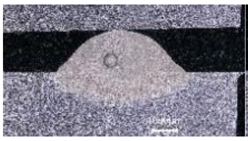
46

47

48
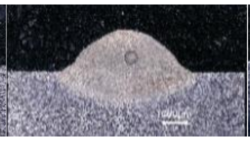
49
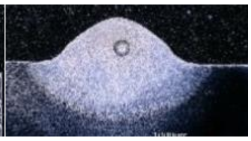
50


51
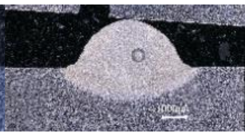
52

53
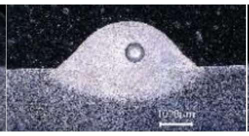
54
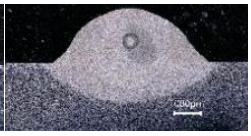
55


56

57

58

59
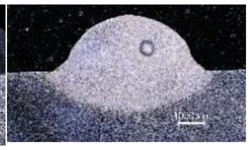
60


61
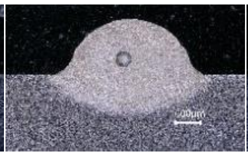
62

63
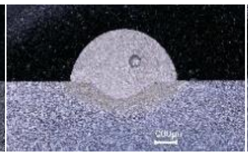
64
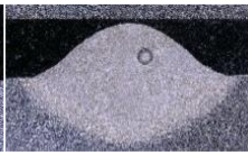
65


66
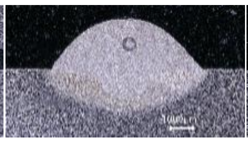
67

68

69
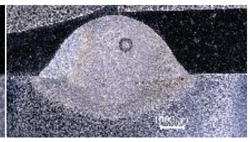
70

71 ***72*** ***73*** 74 ***75***

76 ***77*** ***78*** ***79*** ***80***

81 ***82*** ***83*** 84 ***85***

86 87 ***88*** 89 ***90***

91 ***92*** ***93*** ***94*** ***95***

96 ***97*** ***98*** 99 ***100***

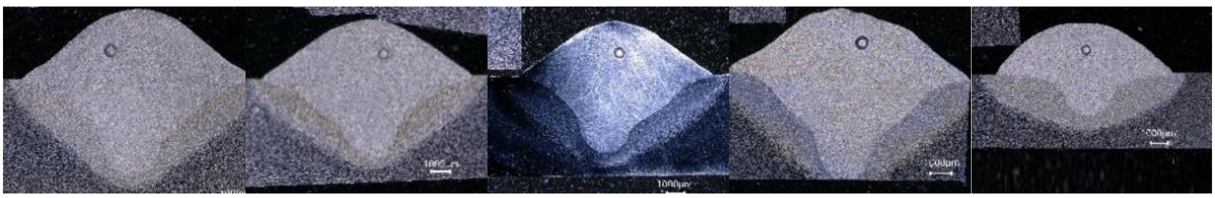

101 ***102*** ***103*** ***104*** ***105***

106

107

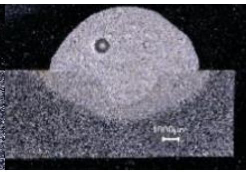

108

109

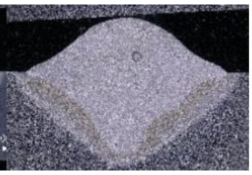

110

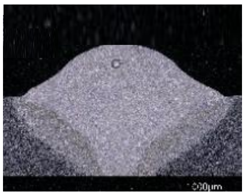

111

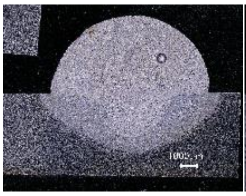

112

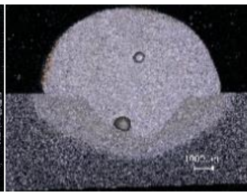

113

114

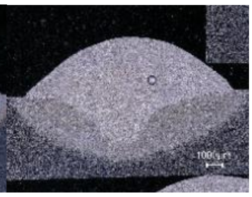

115

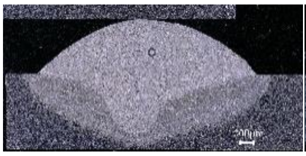

116

117

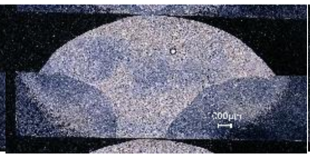

118

119